AFRL-AFOSR-JP-TR-2024-0042

Development of a superconducting hybrid optomechanical system

Vibhor Singh
INDIAN INSTITUTE OF SCIENCE
C V RAMAN AVENUTE, SCIENCE INSTITUTE POST OFFICE,
BANGALORE, KARNATAKA, 560012
IND

01/17/2024
Final Technical Report

Air Force Research Laboratory
Air Force Office of Scientific Research
Asian Office of Aerospace Research and Development
Unit 45002, APO AP 96338-5002

REPORT DOCUMENTATION PAGE

PLEASE DO NOT RETURN YOUR FORM TO THE ABOVE ORGANIZATION.

1. REPORT DATE 20240117	**2. REPORT TYPE** Final	**3. DATES COVERED** **START DATE** 20200814	**END DATE** 20230813

4. TITLE AND SUBTITLE
Development of a superconducting hybrid optomechanical system

5a. CONTRACT NUMBER	**5b. GRANT NUMBER** FA2386-20-1-4003	**5c. PROGRAM ELEMENT NUMBER**
5d. PROJECT NUMBER	**5e. TASK NUMBER**	**5f. WORK UNIT NUMBER**

6. AUTHOR(S)
Vibhor Singh

7. PERFORMING ORGANIZATION NAME(S) AND ADDRESS(ES) INDIAN INSTITUTE OF SCIENCE C V RAMAN AVENUTE, SCIENCE INSTITUTE POST OFFICE, BANGALORE, KARNATAKA 560012 IND	**8. PERFORMING ORGANIZATION REPORT NUMBER**

9. SPONSORING/MONITORING AGENCY NAME(S) AND ADDRESS(ES) AOARD UNIT 45002 APO AP 96338-5002	**10. SPONSOR/MONITOR'S ACRONYM(S)** AFRL/AFOSR IOA	**11. SPONSOR/MONITOR'S REPORT NUMBER(S)** AFRL-AFOSR-JP-TR-2024-0042

12. DISTRIBUTION/AVAILABILITY STATEMENT
A Distribution Unlimited: PB Public Release

13. SUPPLEMENTARY NOTES

14. ABSTRACT

We incorporate a fast-flux line for a frequency tunable transmon qubit in 3D cavity architecture. We investigate the flux-dependent dynamic range, relaxation from unconfined states, and the bandwidth of the flux-line. Using time-domain measurements, we probe transmon's relaxation from higher energy levels after populating the cavity with ~ 2.1x104 photons. For the device used in the experiment, we find a resurgence time corresponding to the recovery of coherence to be 4.8 us. We use a fast-flux line to tune the qubit frequency and demonstrate the swap of a single excitation between cavity and qubit mode in 3 ns. It is an order of magnitude better than the promised deliverable. By measuring the deviation in the transferred population from the theoretical prediction, we estimate the bandwidth of the flux line to be ~100 MHz, limited by the parasitic effect in the design.

Hybrid devices based on the superconducting qubits have emerged as a promising platform for controlling the quantum states of macroscopic resonators. The nonlinearity added by a qubit can be a valuable resource for such control. Here we study a hybrid system consisting of a mechanical resonator longitudinally coupled to a transmon qubit. The qubit readout can be done by coupling to a readout mode like in c-QED setup. The coupling between the mechanical resonator and transmon qubit can be implemented by the modulation of the SQUID inductance. In such a tri-partite system, we analyze the steady-state occupation of the mechanical mode when all three modes are dispersively coupled. We use the quantum-noise and the Lindblad formalism to show that the sideband cooling of the mechanical mode to its ground state is achievable. We further experimentally demonstrate that measurements of the thermomechanical motion is possible in the dispersive limit, while maintaining a large coupling between qubit and mechanical mode. Our theoretical calculations suggest that single-photon strong coupling is within the experimental reach in such hybrid devices.

With artificially engineered systems, it is now possible to realize the coherent interaction rate, which can become comparable to the mode frequencies, a regime known as ultrastrong coupling (USC). We experimentally realize a cavity-electromechanical device using a superconducting waveguide cavity and a mechanical resonator. In the presence of a strong pump, the mechanical-polaritons splitting can nearly reach 81% of the mechanical frequency, overwhelming all the dissipation rates. Beyond the USC limit, the steady-state response becomes unstable. We systematically measure the boundary of the unstable response while varying the pump parameters. The unstable dynamics display rich phases, such as self-induced oscillations, period-doubling bifurcation, period-tripling oscillations, and ultimately leading to the chaotic behaviour. The experimental results and their theoretical modelling suggest the importance of residual nonlinear interaction terms in the weak-dissipative regime.

Cavity electromechanical systems are extensively used for sensing and controlling the vibrations of a mechanical mode down to their quantum limit. We demonstrate a flux-coupled electromechanical device, where a qubit-cavity dressed mode is used to achieve a magnetic-field-dependent electromechanical coupling. It is established by performing an electromechanically-induced transparency experiment with a dressed-mode occupation of 6x10-3 photon. We reach the single-photon coupling rate of 60 kHz, which is nearly 1.5% of the mechanical mode frequency. With increase in the pump strength, the dressed-mode shows the signature of \super-splitting", and strong backaction on the mechanical resonator. It is reected in the broadening of the mechanical linewidth by a factor of 42 while using fewer than 1 photon in the dressed mode. The manifestation of strong backaction on the mechanical resonator in the sub-photon regime takes us one step closer to the nonlinear quantum optomechanics regime.

15. SUBJECT TERMS

16. SECURITY CLASSIFICATION OF:			**17. LIMITATION OF ABSTRACT** SAR	**18. NUMBER OF PAGES** 63
a. REPORT U	**b. ABSTRACT** U	**c. THIS PAGE** U		

19a. NAME OF RESPONSIBLE PERSON MICHAEL RICHARDS	**19b. PHONE NUMBER** *(Include area code)* 3152277000

Standard Form 298 (Rev.5/2020)
Prescribed by ANSI Std. Z39.18

Final Report
on
Superconducting Hybrid Optomechanical System

Federal Agency - Air Force Research Laboratory (AFRL)
Proposal No. - 20IOA003
Award No. - FA23B6-20-1-4003

by
Dr. Vibhor Singh
Department of Physics
Indian Institute of Science, Bangalore
(INDIA)

Project Details

Federal Agency: Air Force Research Laboratory (AFRL)

Grant Number: FA23B6-20-1-4003

Project Title: Development of a superconducting hybrid optomechanical system

Principle Investigator: Dr. Vibhor Singh, Associate Professor

Recipient Organization: Indian Institute of Science Bangalore (INDIA)

Submission Date: January 11, 2024

Project Period: Aug 14, 2020 to Aug 13, 2023

Project Duration: 3 years

Final Report: Yes

Main objectives of the project:

1. to demonstrate quantum-ground state of a dispersively coupled micromechanical resonator,
2. to realize fast-tuning ($\sim$30 ns) of a superconducting qubit in Transmon architecture coupled to a 3-dimensional waveguide cavity,
3. to show cavity-mediated coherent coupling between a superconducting qubit and a macroscopic mechanical resonator,
4. to store/retrieve quantum information into/from mechanical vibrations.

Publications from the project:

1. A fast tunable 3D-transmon architecture for superconducting qubit-based hybrid devices, S. Majumder, T. Bera, R. Suresh, V. Singh - *Journal of Low Temperature Physics* (2022)
2. Prospects of cooling a mechanical resonator with a transmon qubit in c-QED setup, S. Majumder, T. Bera, V. Singh - *Physical Review Research* (2022)
3. Instabilities near ultrastrong coupling in an optomechanical cavity S.R. Das, S. Majumder, S.K. Sahu, U. Singhal, T. Bera, V. Singh - *Physical Review Letters 131 (6), 067001*
4. Strong backaction on a mechanical resonator by a few photons, T. Bera and V. Singh, *arXiv:2309.06765 (2023) - Under Review*

Contents

1 Progress Report: August 2020 - August 2021

1.1 Executive summary

We incorporate a fast-flux line for a frequency tunable transmon qubit in 3D cavity architecture. We investigate the flux-dependent dynamic range, relaxation from unconfined states, and the bandwidth of the flux-line. Using time-domain measurements, we probe transmon's relaxation from higher energy levels after populating the cavity with $\approx 2.1 \times 10^4$ photons. For the device used in the experiment, we find a resurgence time corresponding to the recovery of coherence to be 4.8 μs. We use a fast-flux line to tune the qubit frequency and demonstrate the swap of a single excitation between cavity and qubit mode in 3 ns. It is an order of magnitude better than the promised deliverable. By measuring the deviation in the transferred population from the theoretical prediction, we estimate the bandwidth of the flux line to be ≈ 100 MHz, limited by the parasitic effect in the design..

1.2 Introduction

Josephson circuits are the ideal candidates to realize a wide range of quantum technologies. Low dissipation and the ability to implement tailored Hamiltonians in a quantum circuit have led to a wide range of matured platforms, such as quantum-noise limited amplifiers [1, 2, 3], circuit-QED systems [4, 5], and hybrid devices [6]. While a wide variety of interactions can be implemented by designing the static nonlinearity using Josephson junctions [7, 8], a class of interaction Hamiltonians requires the application of resonant or off-resonant pumps [9, 10, 11]. One such application of c-QED platform is towards the hybrid devices, where it can be used as an auxiliary mode. Hybrid systems based on the mechanical oscillators [12, 13, 14, 15], electron spins [16, 17], surface acoustic waves [18, 19, 20], and magnons [21] have been investigated. Recent developments on the hybrid devices, based on electrostatic coupling with the nanomechanical oscillator [22], and with acoustic resonator [23, 24], operating in the number resolved limit have further raised the interest towards the c-QED based hybrid devices [6].

In hybrid devices, often the requirement of high pump power for the enhancement of the parametric coupling, renders the integration of the c-QED system incompatible. In a high power regime, for example, the transmon qubit decouples from the cavity mode and gets excited to the unconfined-states [25]. The critical power necessary to operate the transmon within the few energy-level subspace can be increased by an inductive shunt but not without compromising the underlying non-linearity [26]. Another useful feature would be the ability to adjust qubit-cavity coupling from dispersive to resonant limits by rapidly tuning the qubit frequency with magnetic flux. While such fast-flux bias lines are straightforward to design in planer devices, integrating them into the 3D-cavity is challenging [27, 28].

With these challenges in mind, investigating the performance of transmon qubit in 3D architecture with a fast-flux line could still have practical importance [29, 30, 31, 32, 33, 34]. For example, consider a low frequency mechanical oscillator coupled to a microwave cavity. In such a device, the re-thermalization time, defined as the time taken to reach the mean phonon occupation of one after initialization to the quantum ground state, can be large due to the high quality factor of the mechanical oscillator. Therefore in a hybrid device, if the relaxation time of the qubit from unconfined states remains smaller than the re-thermalization time, both the systems, qubit and the mechanical oscillator can be initialized to their quantum ground state without a significant loss to the state fidelity. Thus, such initialization in the quantum limit can be used for controlled interaction between the two modes.

1.3 Technical details and results

We incorporate a fast-flux line for a frequency tunable transmon qubit in 3D cavity architecture. We investigate three aspects of such design which is required for the hybrid devices. The dynamic range of the system for various flux bias is probed first. We measure the timescale associated with the recovery of coherence in the system after a strong pump as the transmon relaxes from highly excited states and pump photon leaves the cavity. The initialization to the ground state is probed by performing vacuum-Rabi measurements while varying the delay between the pump and the control signals. Finally, the fast-flux is used to demonstrate the single excitation swap between the cavity and transmon mode.

Unlike the conventional 3D transmon the position of the SQUID loop is shifted away from the center of the cavity into a recess created in the cavity wall[35, 36]. As shown in Fig. 1(a), the SQUID is shifted to a recess designed inside the cavity wall. An antenna pointing towards the cavity center provides the necessary capacitance to the qubit mode and the coupling to the cavity mode. The transmon design was simulated using the black-box quantization technique [37]. Positioning the SQUID loop in a recess allows us to incorporate a local flux line near the SQUID loop to tune the qubit frequency rapidly. Such integration is also compatible with high coherence cavities designed from superconductors [27, 28, 38]. The flux control line is designed to avoid any perturbation to the cavity mode while minimizing the relaxation of qubit mode to the flux-drive port. Fig. 1(b) shows an optical microscope image of the fabricated device using the shadow evaporation technique on an intrinsic silicon substrate. Fig. 1(c) shows the scanning electron microscope image of the SQUID loop. The patterned device is placed inside an oxygen-free high thermal conductivity (OFHC) copper cavity and cooled down to 20 mK. Our measurement setup consists of various absorptive/reflective filters. We use a 1 GHz low-pass reflective filter on the flux-line and place it close to the flux drive port. The entire cavity assembly is placed inside the magnetic and infrared radiation shields.

We begin by performing spectroscopy measurements on the device. Fig. 1(d) shows the cavity spectroscopy measurement as the magnetic flux through the SQUID loop is changed by varying the current through the flux-line. An avoided crossing, signifying the strong coupling, between the qubit mode and the cavity mode is clearly visible. From the qubit spectroscopy, shown in Fig. 1(e), we determine the maximum qubit frequency (ground to first excited state transition) to be $\omega_q^0/2\pi \sim 7.203$ GHz and corresponding dressed cavity frequency for the ground state as $\omega_c/2\pi \sim 5.996$ GHz. We measure the coupling between two modes to be $g/2\pi \sim 87$ MHz, which is close to the designed value [37]. While the maximum qubit frequency depends on the total critical current of the two

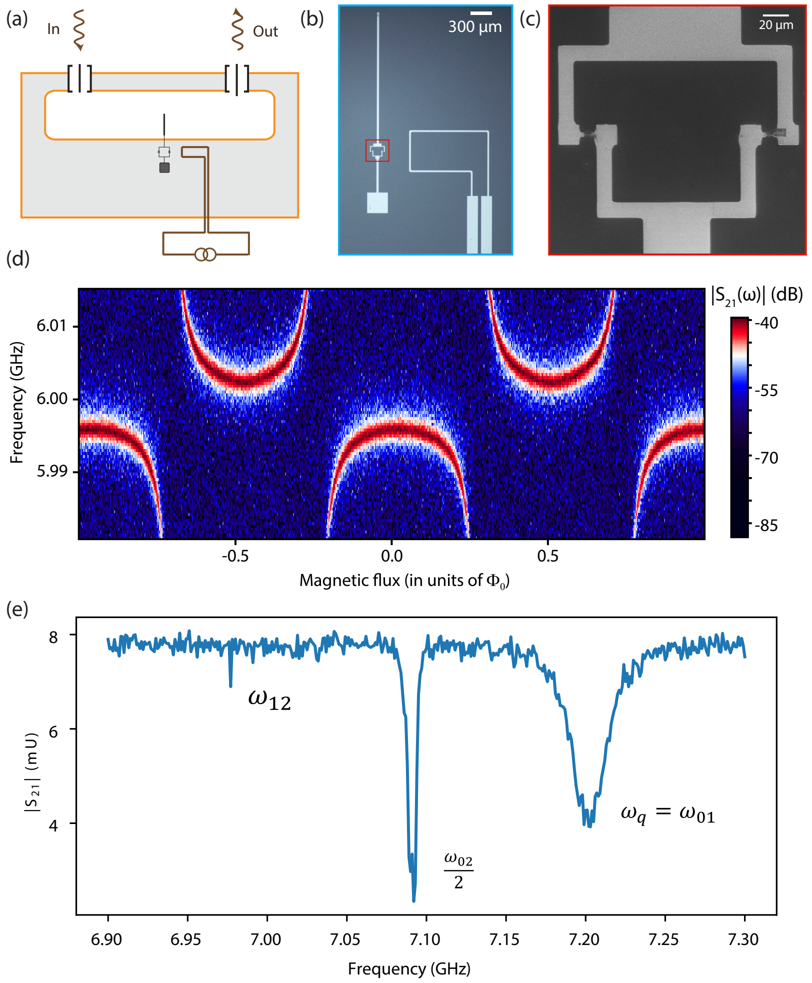

Figure 1: (a) A schematic of the device showing frequency tunable transmon qubit coupled to a 3D cavity. The SQUID loop is positioned in a small recess machined inside the cavity wall to incorporate a port for flux tuning. (b) An optical image of the sample showing the fabricated transmon qubit and the flux line. The thin vertical electrode provides the necessary qubit capacitance and couples to the fundamental mode of the 3D cavity. (c) Scanning electron microscope image of the SQUID loop. (d) Transmission through the cavity $|S_{21}|$ as the magnetic flux threaded by the SQUID loop is varied. (e) Qubit spectroscopy at the high drive power when qubit is flux biased at $\Phi = 0$. Various qubit transitions are labeled accordingly. We determine the qubit anharmonicity to be ≈ 225 MHz.

Device parameter	Symbol	Value
Bare cavity frequency	$\omega_c^0/2\pi$	6.002 GHz
Maximum qubit frequency	$\omega_q^0/2\pi$	7.203 GHz
Kerr-nonlinearity	$\alpha_q/2\pi$	-225 MHz
Maximum Joesphson energy	E_J^0/h	30.65 GHz
Cavity linewidth at zero flux	$\kappa/2\pi$	1.38 MHz
Qubit relaxation time at zero flux	T_1	2.11 μs
Qubit cavity coupling	$g/2\pi$	87 MHz

Table 1: Summary of device parameters studied in the main text

junctions, the minimum qubit frequency depends on the asymmetry of the two junctions. From the two-tone spectroscopy measurements, we could tracked the qubit frequency down to 4 GHz while tuning it with the flux. Various device parameters are summarized in Table 1.

At low probe power, the cavity frequency shifts to a dressed frequency due to its interaction with the qubit. Beyond a critical power, the cavity jumps to its bare frequency defining the dynamic range of the system. In this limit, the phase difference across the junctions evolves continuously. This has been attributed to the excitation of the qubit to the unconfined states lying outside the cosine potential well [25]. We use scqubits package to compute the energy eigen-states using the measured device parameters and find that there are approximately 10 confined states within the cosine potential well [39]. The higher transmon levels exhibit larger charge dispersion [40]. At large probe powers, the higher transmon levels become important, and the coupled system must be treated by including the Kerr-nonlinearity terms. In the dispersive limit, the Hamiltonian of the system can be written as $\hat{H}_{sys}/\hbar = \omega_c\hat{a}^\dagger\hat{a} + \omega_q\hat{b}^\dagger\hat{b} - \frac{1}{2}\alpha_c\hat{a}^\dagger\hat{a}^\dagger\hat{a}\hat{a} - \frac{1}{2}\alpha_q\hat{b}^\dagger\hat{b}^\dagger\hat{b}\hat{b} + \chi\hat{a}^\dagger\hat{a}\hat{b}^\dagger\hat{b}$, where ω_c (ω_q) is the cavity (transmon) frequency, α_c (α_q) is the cavity (transmon) Kerr-nonlinearity and χ is the dispersive shift. Due to the qubit-induced Kerr-nonlinearity, even in the dispersive regime the dynamic range of the cavity gets limited significantly. Fig. 2(a) shows the experimental results of the change in the dressed cavity frequency with probe power at the device. As the probe power is increased, the dressed cavity frequency changes as $\omega_c(\bar{n}) = \omega_c(0) - 2\alpha_c\bar{n}$ [11], where $\bar{n}$ is average number of photons in the cavity. From an independent calibration of $\bar{n}$ using ac-Stark shift, we deduce α_c for different qubit detunings. Additional dataset on ac-Stark shift is included in SI. For zero magnetic flux ($\Phi\ =\ 0$), when qubit detuning $\Delta = \omega_q - \omega_r \approx 2\pi\times 1.2$ GHz, we estimated the the cavity non-linearity to be $\alpha_c/2\pi = -3.2$ kHz. As the qubit mode is tuned closer to the cavity $\Delta = -2\pi\times$ 600 MHz, $\alpha_c/2\pi$ increases to -27.8 kHz, which is also indicated by the reduced dynamic range shown in the Fig. 2(a). As expected, the maximum dynamic range is achieved when the qubit is detuned furthest to the cavity frequency at $\Phi/\Phi_0 = 0.5$. At this flux-operating point, we also observe a reduction in the cavity frequency resulting from the asymmetry in the critical currents of the SQUID junctions. Similar behavior is observed in the corresponding quality factor of the dressed mode, as shown in the Fig. 2(b).

After the basic characterization of the device, we investigate the high power response in the time domain. The high pump power excites the qubit to unconfined states. It

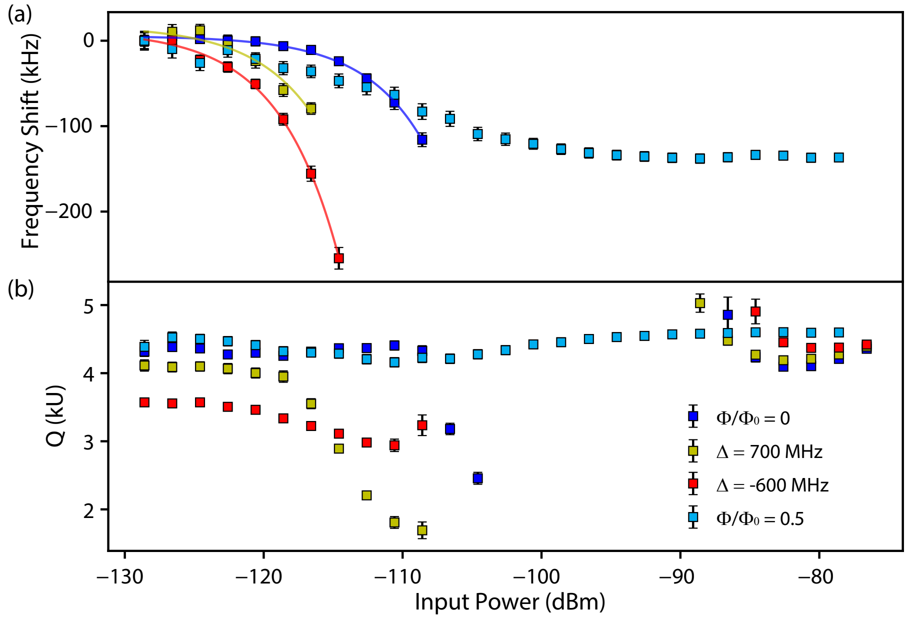

Figure 2: (a) Shift in the dressed cavity frequency as the input power to the cavity is increased for variable magnetic flux. The minimum power -129 dBm corresponds to the mean cavity occupation of 0.17 photons. The solid lines are numerical fits to extract the cavity nonlinearity. (b) The loaded (total) quality factor of the dressed mode for different input power to the cavity at multiple flux bias points.

could be accompanied by the creation of quasi-particles, which could take a long time to relax. We perform time-domain measurements to probe the resurgence of coherence after subjecting the system to a strong pump.

Using the flux-bias, the qubit frequency is tuned to the maximum frequency $\Delta = \omega_q - \omega_r \approx 2\pi\times 1.2$ GHz. A control pulse at the qubit frequency is applied. It is followed by a measurement pulse at the dressed cavity frequency, corresponding to a steady-state cavity occupation of $\approx$ 5 photons. The transmitted signal from the cavity is amplified at 4 K and at room temperature. The amplified signal is then down-converted to an intermediate frequency. Both quadratures of the IF signal are recorded as a function of time with a lock-in amplifier. To improve the readout signal contrast, we average fifty thousand time-traces of in-phase and quadrature streams of the readout signal.

Such an ensemble average of time traces can then be used to determine the qubit state. We follow an approach similar to Ref. [41] and define a normalized integrated signal V_H as $V_H = \frac{1}{2}\frac{\sum_i (V_g(t_i)-V_m(t_i))\Delta t}{\sum_i (V_g(t_i)-V_s(t_i))\Delta t}$, where Δt is the resolution of time-axis. V_g (V_s) represents the averaged signal traces corresponding to the qubit in the ground state (in an equal mixture of ground and the first excited state). V_m represents signal for the unknown qubit state that is being measured. Here, we effectively use the saturation control pulse for normalization. It is important to emphasize here that V_H slightly deviates from the first excited state probability due to loss of population during the measurement process.

To probe the relaxation of qubit from the higher energy levels to the ground state, a strong pump tone is applied at the bare cavity frequency, followed by the pulsed control

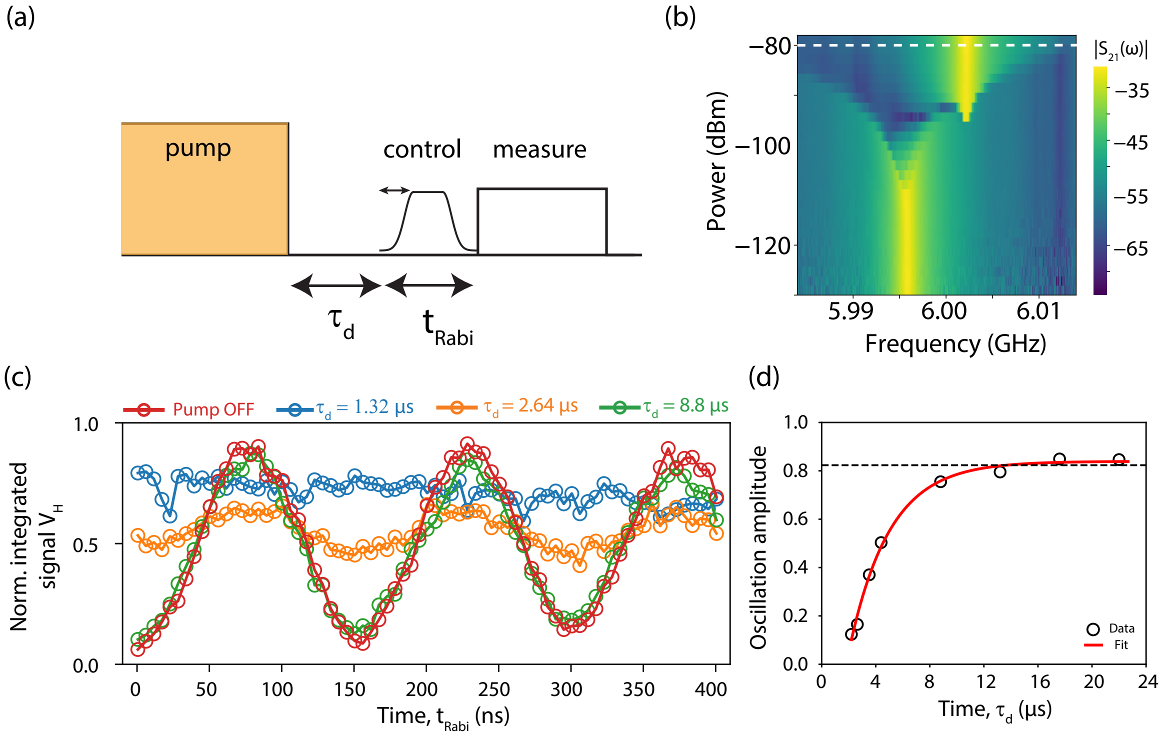

Figure 3: (a) A schematic of the pulse sequence used in the measurement. The cavity is driven with a strong pump pulse, which creates a large population of photons in the cavity and excites the transmon to unconfined states. Subsequently, Rabi measurement protocol with varying delays τ_d is followed. For control, we use a pulse that has a rise and fall parts defined by a gaussian function and central part of the pules is rectangular. The rise (and fall) part of the pulse is defined by a Gaussian function of length 35 ns and a σ of 9 ns, indicated by the arrow. (b) Cavity transmission as probe power is increased while biasing the qubit at zero flux quantum. The white dotted line indicates the power used for the high power pulsed measurements. (c) Rabi measurement for different delays between the high power pump and qubit control pulse. A plot of Rabi oscillation without any high power pump is included as a reference. The pump power in the steady-state corresponds to a photon number n_d of 2.1×10^4. (d) Amplitude of Rabi oscillation measured for different delays between the pump and the control pulse. Oscillation amplitude when the pump pulse is in off condition is denoted by the black dotted line. Statistical uncertainties from the fits are smaller than the marker size.

and readout scheme as described before. A schematic of the pulse sequence is shown in Fig. 3(a). In the presence of a strong pump, the transmon gets excited to the unconfined states resulting in the maximum transmission through the cavity at its bare frequency. Fig. 3(b) shows the measurement of transmission through the cavity as power of the probe signal is increased. The dressed mode shows the characteristic frequency shift due to the presence of the qubit. Beyond a critical power, the maximum transmission jumps to the bare cavity frequency. For the pump pulse, corresponding mean occupation of n_d $\sim$2.1$\times$10^4 photons in the cavity indicated by the dotted line in Fig. 3(b). The calibration of the pump photons is performed by using the ac Stark measurements made at low probe powers. We have calibrated the total attenuation in the line and calculated the total number of photon with respect to bare cavity frequency. This strong pump pulse excites the qubit to higher unconfined states. By varying the length of the qubit control pulse, we perform the vacuum Rabi-oscillation measurement for different delay time (τ_d) between the pump and qubit control.

Fig. 3(c) shows the measurements of normalized integrated signal V_H for different delays. The horizontal axis corresponds to the duration of the qubit control pulse. For comparison, a measurement made in the absence of the pump pulse is included as well. For $\tau_d = 2.64$ μs, we see small oscillations in the measurement indicating the coherent pouplation transfer between the ground and the first excited state. For such short delay time τ_d, there are two effects that reduce the contrast of oscillations. First, the qubit population in the ground or first excited state could be low due to its excitation to higher levels. Second, for short times, the pump photon occupancy in the cavity can be substantial leading to dephasing. We use slowly varying control pulse and therefore rule out any leakage of qubit to the higher levels by the control pulse. For $\tau_d = 8.8$ μs, the oscillations closely resemble the result obtained with pump maintained in off-condition. We systematically measure the amplitude of Rabi oscillations for different delay time between pump and the control pulse. Fig 3(d) shows the plot of oscillation amplitude for different delay times, showing the clear resurgence of the coherence in the device. Additional dataset is included in the SI. By fitting it to $\mathcal{F}(1 - e^{\frac{t-t_0}{\tau}})$, we extract the characteristic timescale, $t_0 + \tau \approx 4.8$ μs for the relaxation from unconfined states. We point out here that such a timescale involves contributions from the relaxation of qubit from the higher excited states and from the dephasing due to occupancy of the cavity by pump-photons.

After characterizing the response of the device under high power, next, we perform the characterization of the flux bias port. We utilize the high bandwidth of the flux drive line and create a single-photon state in the cavity. The pulse protocol for such scheme is shown in Fig. 4(a). It consists of initializing the qubit to the first excited state by applying a π-pulse. The qubit frequency is then rapidly tuned to bring it in resonance with the cavity. The modes are maintained in resonance for a variable time τ_{int} and then the qubit mode is brought back to the original frequency followed by a measurement pulse. During the interaction period, the qubit and the cavity modes exchange the single excitation coherently. To understand the applicability of this scheme in a strongly driven system, we follow this protocol after a strong pump (at the bare cavity frequency) pulse with varied delay time τ_d.

The current in the flux loop, controlling the qubit detuning, is applied using an

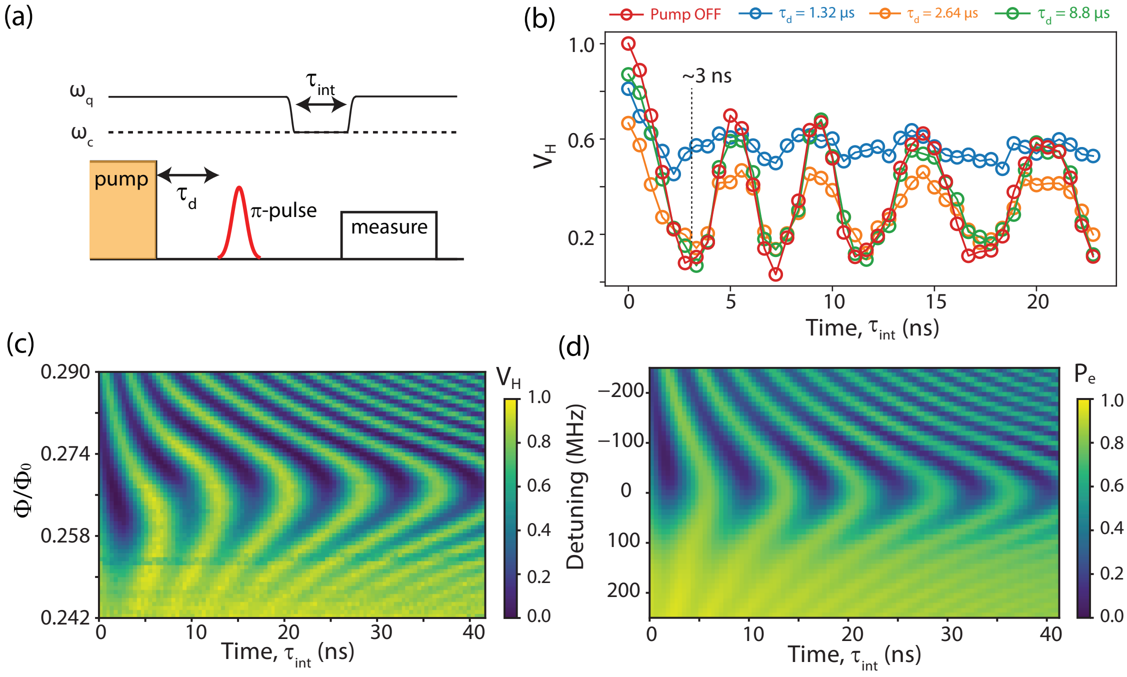

Figure 4: (a) A schematic of the pulse sequence used in the measurement. The interaction time (τ_{int}) between cavity and qubit is varied for different values of τ_d. (b) Normalized integrated signal showing the swap of excitation between the qubit and the cavity mode as the interaction length is varied. The black dotted line indicates the time to swap one excitation. (c) The colorplot of the normalized integrated signal as the detuning between the cavity mode and qubit is varied. The results were obtained from a different device with similar parameters. (d) The colorplot of the simulated qubit population in the excited state while varying the interaction length and relative detuning $\Delta = \omega_q - \omega_c$.

arbitrary waveform generator. The shape of the flux-pulse is rectangular with rising and falling segments set as the half-gaussian with standard deviation of 1.1 ns. The width and the amplitude of the flux pulse are varied to control the interaction time and the qubit frequency, respectively. Fig. 4(b) shows V_H as the interaction length is varied. For delay time of 8.8 μs ($> t_0 + \tau$), we observe that the qubit regains the coherence and oscillation due to the swapping of a single excitation can be clearly seen. Due to the strong coupling between the qubit and the cavity, it takes approximately 3 ns to transfer the single-photon from the qubit mode to the cavity mode indicated by the black dotted line.

Fig. 4(c) shows the colorplot of V_H as the qubit detuning and interaction duration is varied. The oscillation frequency of the single excitation swap changes as the relative detuning between the qubit and cavity mode frequency is varied. At zero detuning, the oscillation frequency is minimum at $2g$ and increases to $\sqrt{4g^2 + \Delta^2}$ with detuning [13]. The deviation from the ideal chevron pattern suggests that the flux-pulse disperses as it travels down the sample. The initial change in the flux pulse is not able to tune the qubit in resonance with the cavity for short interaction time. We observe a small distortion in the chevron pattern for time-scales shorter than 10 ns. From this deviation, we concluded the bandwidth of the flux-line to be approximately 100 MHz. The bandwidth of flux line is limited by the parasitic capacitance and self-inductance of the current loop patterned near the SQUID loop. While we try to maintain a 50 Ω environment till the connector on the cavity, the impedance of the flux line on the silicon chip deviates from 50 Ω and this limits the bandwidth. Such distortions in flux-pulse, in principle, could be improved by using pre-compensated flux-pulses. To better understand the experimental results, we numerically simulate the system by solving the Lindblad master equation with the flux pulse sequence used in the experiment [42]. The simulated outcome of the excited state population is plotted in Fig. 4(d) with variable detuning in the vertical axis. The difference between the simulation and experimental plots can be understood from the distorted flux-pulse at the sample, as discussed above.

To summarize, we demonstrated a design of a fast-tunable transmon qubit in a 3D waveguide cavity architecture. We characterized its relaxation from unconfined states to the ground state after a high power drive pulse. We measure a resurgence time of 4.8 μs. We characterize the fast-flux line and find a bandwidth of $\approx$ 100 MHz. These performance benchmarking results provide the design guidelines for hybrid systems intended to integrate additional degrees of freedom with the circuit-QED platform [31, 32].

2 Progress report: August 2021 - December 2022

2.1 Executive summary

Hybrid devices based on the superconducting qubits have emerged as a promising platform for controlling the quantum states of macroscopic resonators. The nonlinearity added by a qubit can be a valuable resource for such control. Here we study a hybrid system consisting of a mechanical resonator longitudinally coupled to a transmon qubit. The qubit readout can be done by coupling to a readout mode like in c-QED setup. The coupling between the mechanical resonator and transmon qubit can be implemented by the modulation of the SQUID inductance. In such a tri-partite system, we analyze the steady-state occupation of the mechanical mode when all three modes are dispersively coupled. We use the quantum-noise and the Lindblad formalism to show that the sideband cooling of the mechanical mode to its ground state is achievable. We further experimentally demonstrate that measurements of the thermomechanical motion is possible in the dispersive limit, while maintaining a large coupling between qubit and mechanical mode. Our theoretical calculations suggest that single-photon strong coupling is within the experimental reach in such hybrid devices.

2.2 Introduction

Control over the quantum states of a mechanical resonator by coupling them to optical modes can have several potential applications in the field of quantum technologies [43]. The traditional cavity-optomechanics based approach of coupling a mechanical resonator to an optical mode via the radiation-pressure interaction has been quite successful [44, 45, 46, 47, 48, 32, 49, 50]. While the radiation-pressure mediated coupling in such devices is nonlinear, its magnitude is usually small in the most implementations. Further, due to the dispersive interaction, the effects originating from the Kerr-term are strongly suppressed [51, 52].

To mitigate the limitations of linear cavity optomechanics, hybrid devices based on the strong nonlinearity of qubits have been proposed and developed [53, 8, 6]. These proposals explore their performance from the sideband cooling of the mechanical resonator [54] to the matter-interferometry [55], while considering a wide range of two-level systems such as superconducting qubits [54, 56, 57, 58, 59, 60, 61], quantum-dots [62], and nitrogen vacancy defects in diamond [63]. Particularly, in the microwave domain, experimental realization of several hybrid devices have been shown using the nonlinearity of a superconducting qubit [64], Josephson capacitance [15, 22], Josephson inductance [65, 66, 67, 68], and piezo-electricity [13, 24].

Among these different schemes, the electromechanical coupling stems from charge or flux modulation, and its tunability is controlled by the external parameters. Recently, the magnetic flux-mediated coupling approach have shown promising experimental results [65]. These systems have demonstrated large electromechanical coupling [66, 67, 68], four-wave-cooling of the mechanical resonator to near the quantum ground state [69], and Lorentz-force induced backaction on the mechanical resonator [70].

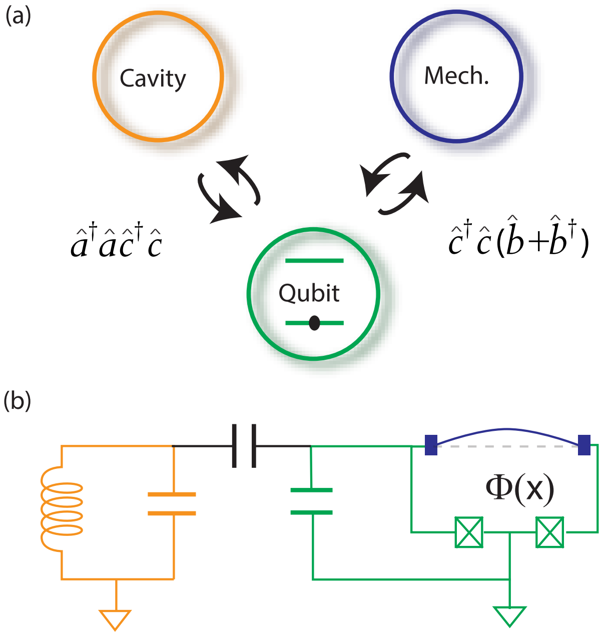

Figure 5: (a) A conceptual schematic of the three-mode hybrid device showing a linear cavity coupled to a qubit which in turn couples to a mechanical resonator. A direct coupling between the cavity and the mechanical mode is not considered. (b) A possible implementation using a frequency tunable transmon qubit, where coupling to mechanical mode is achieved by embedding it the SQUID loop and by applying a constant magnetic field. A magnetic field perpendicular (parallel) to the SQUID loop couples the in-plane (out-of-plane) mechanical mode to the qubit.

Motivated by the progress on flux-mediated approach, here we investigate a coupled three-mode system consisting of a mechanical mode, transmon qubit, and a readout cavity. From the practical point of view, the additional readout cavity is useful ingredient to consider as it allows the quantum non-demolishing (QND) measurement of qubit mode in circuit-QED setup [71, 72]. While a mechanical mode coupled to a two-level system has been studied extensively in the past [54, 73, 56, 53, 74], the focus of our investigation has been on treating the transmon qubit as a weakly anharmonic oscillator. In addition, we theoretically and experimentally address the readout of the mechanical mode when transmon is detuned far away from the readout cavity. This regime is particularly important as large electromechanical coupling with the qubit mode can be achieved. Using the quantum-Langevin equation of motion [75], and Lindblad formalism [76], we analyze the possibility of sideband cooling of the mechanical resonator. Experimentally, we use a two-tone method to measure the thermo-mechanical motion, and compare it with analytical results.

2.3 Theoretical model details

We consider a coupled system where the mechanical mode modulates the transmon qubit frequency, therefore resulting in a longitudinal coupling. Such coupling between transmon qubit and the mechanical resonator can be implemented by embedding a mechanical resonator into the SQUID loop of the qubit. In addition, the qubit couples to a linear mode (the readout cavity) transversely as in the circuit-QED setup. A schematic diagram of the system and a possible implementation with the equivalent circuit diagram are shown in the Fig. 5(a) and (b).

Using the dispersive approximation between the transmon and the readout cavity, we arrive at the following system Hamiltonian:

$$\hat{\mathcal{H}}_0 = \omega_c \hat{a}^\dagger \hat{a} + \omega_q \hat{c}^\dagger \hat{c} - \frac{\alpha_q}{2}\hat{c}^\dagger \hat{c}^\dagger \hat{c}\hat{c} + \omega_m \hat{b}^\dagger \hat{b} + \chi \; \hat{a}^\dagger \hat{a} \hat{c}^\dagger \hat{c} + g_0 \; \hat{c}^\dagger \hat{c}(\hat{b} + \hat{b}^\dagger), \tag{1}$$

where $\hat{a}(\hat{a}^\dagger)$, $\hat{c}(\hat{c}^\dagger)$, $\hat{b}(\hat{b}^\dagger)$ are the annihilation(creation) operators for the cavity, qubit and the mechanical mode of frequency ω_c, ω_q, ω_m, respectively. The Kerr-nonlinearity of the transmon is denoted as α_q. The last two terms are the interaction terms between the modes. The dispersive coupling between the qubit and the readout cavity is denoted by χ. The radiation-pressure type coupling between the transmon and the mechanical mode is denoted by the single photon coupling rate g_0.

Two additional drive terms of amplitude δ and ϵ at frequency of ω_L (near ω_c) and ω_d (near ω_q) are added to the Hamiltonian. The drive Hamiltonian can be written as,

$$\hat{\mathcal{H}}_d = (\delta \hat{a} \; e^{+i\omega_L t} + \epsilon \hat{c} \; e^{+i\omega_d t}) + h.c. \tag{2}$$

By carrying out rotating frame transformations, given by the unitary operators $U^a = \exp\left[i\omega_L \hat{a}^\dagger \hat{a} t\right]$ and $U^c = \exp\left[i\omega_d \hat{c}^\dagger \hat{c} t\right]$, the transformed Hamiltonian can be written as,

$$\hat{\mathcal{H}} = -\Delta_c \hat{a}^\dagger \hat{a} - \Delta_q \hat{c}^\dagger \hat{c} - \frac{\alpha_q}{2}\hat{c}^\dagger \hat{c}^\dagger \hat{c}\hat{c} + \omega_m \hat{b}^\dagger \hat{b} + \chi \; \hat{a}^\dagger \hat{a} \hat{c}^\dagger \hat{c} + g_0 \; \hat{c}^\dagger \hat{c}(\hat{b} + \hat{b}^\dagger) + \delta \; (\hat{a} + \hat{a}^\dagger) + \epsilon \; (\hat{c} + \hat{c}^\dagger), \tag{3}$$

where $\Delta_c = \omega_L - \omega_c$ and $\Delta_q = \omega_d - \omega_q$. In this frame of rotation, the transformed Hamiltonian becomes time-independent. For further analysis, we shift to a mean field frame using the following displacement transformation,

$$\mathcal{D}(\alpha, \mu, \beta) = \exp\left[\alpha(\hat{a} - \hat{a}^\dagger) + \mu(\hat{c} - \hat{c}^\dagger) + \beta(\hat{b} - \hat{b}^\dagger)\right], \tag{4}$$

where α, μ, β are real scalar quantities. For a particular choice of $\alpha = \bar{\alpha}$, $\mu = \bar{\mu}$ and $\beta = \bar{\beta}$, all the drive terms (terms proportional to $\hat{a} + \hat{a}^\dagger$, $\hat{b} + \hat{b}^\dagger$, and $\hat{c} + \hat{c}^\dagger$) get cancelled. After dropping the third and higher order terms, we arrive at the following effective Hamiltonian,

$$\hat{\mathcal{H}}' \approx -\tilde{\Delta}_c \hat{a}^\dagger \hat{a} - \tilde{\Delta}_q \hat{c}^\dagger \hat{c} - \eta(\hat{c}^2 + \hat{c}^{\dagger 2}) + \omega_m \hat{b}^\dagger \hat{b} + J(\hat{a} + \hat{a}^\dagger)(\hat{c} + \hat{c}^\dagger) + g(\hat{c} + \hat{c}^\dagger)(\hat{b} + \hat{b}^\dagger), \tag{5}$$

where $\tilde{\Delta}_c = \Delta_c - \chi\bar{\mu}^2$, $\tilde{\Delta}_q = \Delta_q + 2\alpha_q\bar{\mu}^2 - \chi\bar{\alpha}^2 - 2g_0\bar{\beta}$, $\eta = \frac{\alpha_q\bar{\mu}^2}{2}$, $J = \chi\bar{\alpha}\bar{\mu}$ and $g = g_0\bar{\mu}$. It might be important to underline here that the coupling rates g and J as defined above are the scaled coupling rates. Both the coupling rates, g and J, show the scaling with drive tone amplitude similar to the case in linear optomechanical device.

2.4 Equations of motion

Dynamics of the system depends on various decay rates associated with different modes and drive amplitudes. We write the equations of motion for the field operators while incorporating all the noise operators and decay rates as,

$$\dot{\hat{a}} = -i\left[\hat{a}, \hat{\mathcal{H}}'\right] - \frac{\kappa}{2}\hat{a} + \sqrt{\kappa_{ex}}\ \hat{a}_{in} + \sqrt{\kappa_0}\ \hat{f}_{in}, \tag{6a}$$

$$\dot{\hat{c}} = -i\left[\hat{c}, \hat{\mathcal{H}}'\right] - \frac{\Gamma}{2}\hat{c} + \sqrt{\Gamma_{ex}}\ \hat{c}_{in} + \sqrt{\Gamma_0}\ \hat{\xi}_{in}, \tag{6b}$$

$$\dot{\hat{b}} = -i\left[\hat{b}, \hat{\mathcal{H}}'\right] - \frac{\gamma_m}{2}\hat{b} + \sqrt{\gamma_m}\ \hat{b}_{in}, \tag{6c}$$

where $\hat{a}_{in}$, $\hat{c}_{in}$, $\hat{b}_{in}$, $\hat{f}_{in}$, $\hat{\xi}_{in}$ are the noise operators of cavity, qubit and mechanical mode, respectively. The mechanical energy dissipation rate is γ_m. The internal, external and total cavity (qubit) dissipation rates are κ_0 (Γ_0), κ_{ex} (Γ_{ex}), and κ (Γ), respectively. This set of equations can be solved by performing a Fourier transformation, defined as $x[\omega] = \mathcal{F}\left[x(t)\right] = \int_{-\infty}^{+\infty} x(t)\mathrm{e}^{i\omega t}\mathrm{d}t$, of the equations. We now define a field vector $u[\omega] = \left[\hat{a}[\omega], (\hat{a}^{\dagger})[\omega], \hat{c}[\omega](\hat{c}^{\dagger})[\omega], \hat{b}[\omega], (\hat{b}^{\dagger})[\omega]\right]^T$ and evaluate its governing equation of the form,

$$u[\omega] = (-i\omega\mathbb{I} - A)^{-1}\ r[\omega] = \mathcal{B}\ r[\omega], \tag{7}$$

where,

$$r[\omega] = \begin{bmatrix} \sqrt{\kappa_{ex}}\ \hat{a}_{in}[\omega] + \sqrt{\kappa_0}\ \hat{f}_{in}[\omega] \\ \sqrt{\kappa_{ex}}\ (\hat{a}_{in}^{\dagger})[\omega] + \sqrt{\kappa_0}\ (\hat{f}_{in}^{\dagger})[\omega] \\ \sqrt{\Gamma_{ex}}\ \hat{c}_{in}[\omega] + \sqrt{\Gamma_0}\ \hat{\xi}_{in}[\omega] \\ \sqrt{\Gamma_{ex}}\ (\hat{c}_{in}^{\dagger})[\omega] + \sqrt{\Gamma_0}\ (\hat{\xi}_{in}^{\dagger})[\omega] \\ \sqrt{\gamma_m}\ \hat{b}_{in}[\omega] \\ \sqrt{\gamma_m}\ (\hat{b}_{in}^{\dagger})[\omega] \end{bmatrix} \tag{8}$$

The matrix $\mathcal{B}$ can be calculated from Eq. (18) and Eq. (6) as,

$$\mathcal{B} = \begin{bmatrix} 1/\chi_c & 0 & iJ & iJ & 0 & 0 \\ 0 & 1/\tilde{\chi}_c & -iJ & -iJ & 0 & 0 \\ iJ & iJ & 1/\chi_q & -2i\eta & ig & ig \\ -iJ & -iJ & 2i\eta & 1/\tilde{\chi}_q & -ig & -ig \\ 0 & 0 & ig & ig & 1/\chi_m & 0 \\ 0 & 0 & -ig & -ig & 0 & 1/\tilde{\chi}_m \end{bmatrix}^{-1}. \tag{9}$$

All χ's in the matrix represent the susceptibility of the modes, defined as,

$$\chi_c[\omega] = \frac{1}{-i\omega - i\tilde{\Delta}_c + \frac{\kappa}{2}};\ \tilde{\chi}_c[\omega] = \frac{1}{-i\omega + i\tilde{\Delta}_c + \frac{\kappa}{2}}$$

$$\chi_q[\omega] = \frac{1}{-i\omega - i\tilde{\Delta}_q + \frac{\Gamma}{2}};\ \tilde{\chi}_q[\omega] = \frac{1}{-i\omega + i\tilde{\Delta}_q + \frac{\Gamma}{2}}$$

$$\chi_m[\omega] = \frac{1}{-i\omega + i\omega_m + \frac{\gamma_m}{2}};\ \tilde{\chi}_m[\omega] = \frac{1}{-i\omega - i\omega_m + \frac{\gamma_m}{2}}.$$

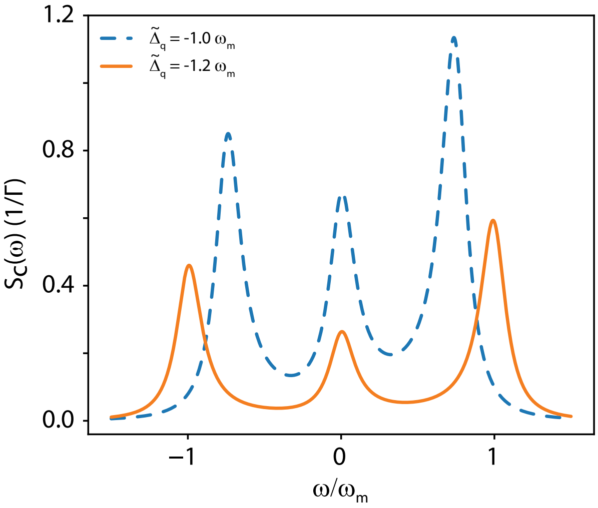

Figure 6: Plot of the qubit spectrum for two different values of drive detunings, $\tilde{\Delta}_q = -1.0\ \omega_m$ (dashed blue line) and $\tilde{\Delta}_q = -1.2\ \omega_m$ (solid orange line). The parameters used for the plots are: $\tilde{\Delta}_c = 0$, $\omega_m = 2\pi \times 6$ MHz, $J = 2\pi \times 0.8$ MHz, $g = 2\pi \times 2$ kHz, $\kappa = 2\pi \times 4$ MHz, $\omega_m/\Gamma = 5$, $\gamma = 2\pi \times 6$ Hz, and $\eta = 2\pi \times 2$ MHz.

From Eq. 7, we can solve for the field operators. Further, we define the spectrum of any mode as,

$$S_{\mathcal{O}}(\omega) = \frac{1}{2\pi}\int_{-\infty}^{+\infty} \langle (\hat{\mathcal{O}}[\omega'])^{\dagger}\hat{\mathcal{O}}[\omega]\rangle \mathrm{d}\omega'. \tag{10}$$

Eq. 10 and the solution of field operators can be used to get the spectrum of the modes. The detailed calculations and the correlators of noise operators are given in Appendix **A**. The calculated spectrum as follows,

$$S_{\mathrm{x}}(\omega)\Big|_{\mathrm{x}\epsilon\{1,3,5\}} = n_m^i\gamma_m(|\mathcal{B}_{\mathrm{x}5}[\omega]|^2 + |\mathcal{B}_{\mathrm{x}6}[\omega]|^2) + \kappa|\mathcal{B}_{\mathrm{x}2}[\omega]|^2 + \Gamma|\mathcal{B}_{\mathrm{x}4}[\omega]|^2 + \gamma_m|\mathcal{B}_{\mathrm{x}6}[\omega]|^2, \tag{11}$$

where n_m^i is the initial phonon occupation in the mechanical mode. The indexing $\{S_1, S_3, S_5\}$ maps to the spectrum of cavity, qubit and mechanics as $\{S_a, S_c, S_b\}$, respectively.

2.5 Spectrum of the qubit and the mechanical mode

In this section, we discuss the best cooling scenario of the mechanical resonator by inspecting the qubit and the mechanical spectrum. Fig. 6 shows the spectrum of the transmon qubit for two different detuning of the drive tone $\tilde{\Delta}_q = -1.0\ \omega_m$ (dashed blue line) and $\tilde{\Delta}_q = -1.2\ \omega_m$ (solid orange line). In presence of a the nearly red detuned drive on qubit mode, its spectrum becomes asymmetric. The cooling rate is calculated from the asymmetry of the spectrum, which is large for a specific drive position. In the weak coupling regime ($g << \Gamma$), the cooling rate for the mechanical resonator is given by $\Gamma_c = 2[g^2(S_c(\omega_m) - S_c(-\omega_m)) + \gamma_m]$ [56, 53]. The optimum cooling rate, as seen from

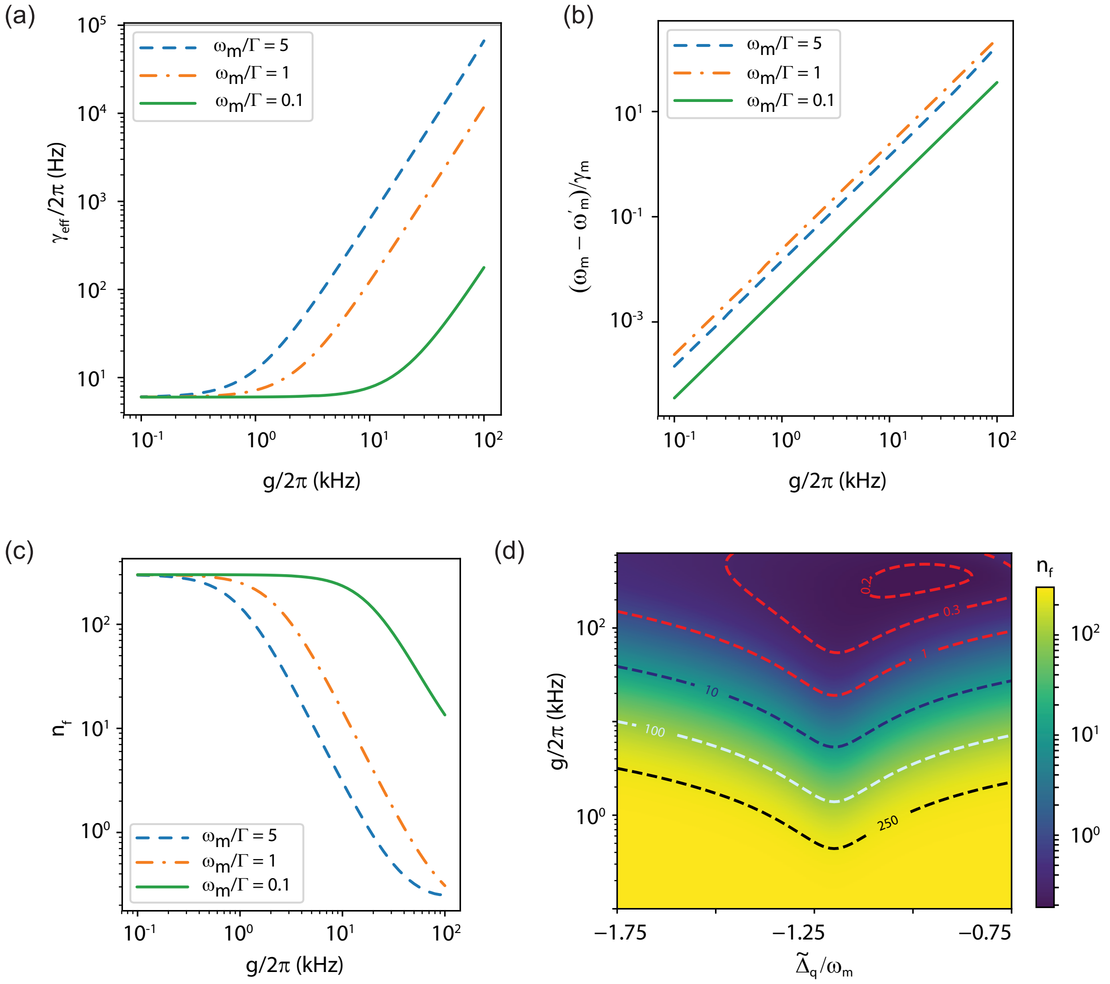

Figure 7: **Cooling of the mechanical mode:** The spectrum of the mechanical mode is analyzed to characterize the effect of back action arising from the drive tone near the qubit frequency ω_q. The extracted parameters for effective mechanical linewidth and shift in the mechanical resonant frequency as the electromechanical coupling between the qubit and the mechanical mode is varied, are shown in (a) and (b). Panel (c) shows the final phonon occupancy (n_f) of the mechanical mode. It is extracted by calculating the area under the Lorentzian in mechanical spectrum. For large qubit-mechanics coupling a final phonon occupation well-below 1 can be achieved for various sideband parameters. The dashed, dotted dash, and solid lines correspond to $\omega_m/\Gamma = 5$, $\omega_m/\Gamma = 1$, and $\omega_m/\Gamma = 0.1$, respectively. (d) Final phonon occupancy as a function of qubit-mechanics coupling and scaled detuning between the drive and the qubit frequency for $\omega_m/\Gamma = 5$. The parameters used for the plots are: $\tilde{\Delta}_c = 0$, $\omega_m = 2\pi \times 6$ MHz, $J = 2\pi \times 0.8$ MHz, $\eta = 2\pi \times 2$ MHz, $\kappa = 2\pi \times 4$ MHz, $\gamma = 2\pi \times 6$ Hz, $n_m^i = 300$. For the plot in panel (a), (b), and (c), we use $\tilde{\Delta}_q = -1.2\ \omega_m$ as the detuning.

Fig. 6, is a function of the position of the drive [56]. Unlike a linear cavity as a bath for cooling, the cooling rate of a mechanical resonator for an anharmonic oscillator (the qubit) depends on the position of the cooling tone applied and the anharmonicity of the resonator mode. This is a direct consequence of the Kerr-term. In the steady state, the final phonon occupancy can be calculated from the cooling rate and the qubit spectrum as,

$$n_f = 2\frac{n_m^i \gamma_m}{\Gamma_c} + 2g^2 \frac{S_c(-\omega_m)}{\Gamma_c}. \tag{12}$$

To further understand the backaction on the mechanical resonator due to a drive on the qubit mode, we compute the mechanical spectrum $S_b(\omega)$. In the steady state, the mean phonon occupancy of the mechanical mode can be calculated as $n_f = \frac{1}{2\pi}\int S_b(\omega)d\omega$, which is the area under the Lorentzian in the mechanical mode spectrum. While it is possible to reduce the expression of the mechanical spectrum to a Lorentzian form, we find it more efficient to compute the spectrum and carry out a numerical fit to extract the effective linewidth and the effective resonant frequency. Fig. 7(a) and Fig. 7(b) show the linewidth broadening and resonant frequency shift of the mechanical mode, for a red detuned ($\tilde{\Delta}_q = -1.2\ \omega_m$) qubit drive. The back-action on the mechanical resonator from the drive on qubit is reflected in the change of mechanical frequency and an increase in the effective linewidth. The final phonon occupation is plotted in Fig. 7(c) for different value of sideband parameter ω_m/Γ. It is evident from the figure that in the steady driving of the qubit, the final phonon occupancy strongly depends on sideband parameter ω_m/Γ. A larger value of sideband parameter offers better cooling of the mechanical mode. It is important to underline here that the cooling to the quantum ground state of the mechanical resonator is possible well before entering the strong coupling regime, $g \gtrsim \max(\Gamma, \kappa)$.

To gain insight into the spectrum calculation, we consider a simpler case when qubit anharmonicity is set to zero $\eta = 0$, and it is being driven at the lower mechanical sideband $\tilde{\Delta}_q = -\omega_m$. With these parameters and Eq. 10, the mechanical spectrum can be approximately written as,

$$S_b(\omega) = \frac{n_m^i \gamma_m \Gamma^2/(\Gamma^2 - 8g^2)}{(\omega - \omega_m)^2 + \frac{(4g^2+\gamma_m\Gamma)^2}{4(\Gamma^2-8g^2)}}. \tag{13}$$

From this simplified expression of the mechanical spectrum, we can write the effective line-width of the mechanical resonator as, $\gamma_{eff} = \frac{4g^2+\gamma_m\Gamma}{\sqrt{\Gamma^2-8g^2}} \simeq \gamma_m(C+1)$, where $C = \frac{4g^2}{\gamma_m\Gamma}$ is defined as the cooperativity. Similarly, the final mean phonon occupation can be written as, $n_f = \frac{n_m^i\gamma_m\Gamma^2}{4g^2+\gamma_m\Gamma}\frac{1}{\sqrt{\Gamma^2-8g^2}} \simeq \frac{n_m^i}{1+C}$ for $\Gamma \gg g$. We note that in the limit of zero anharmonicity and weak coupling, the results are consistent with that obtain from linear cavity optomechanics [44].

For the model Hamiltonian given by Eq. 18, the mean phonon-occupation can also be obtained by solving Lindblad master equation. Here, we obtain the equations of motion for the expectation values of mode operators and solve for the steady-state solutions. From this formalism, we calculate the steady-state occupancy in the mechanical mode for the various drive detuning $\tilde{\Delta}_q$ and coupling g. Fig. 7(d) shows the color plot of the final phonon occupation for the sideband parameter of $\omega_m/\Gamma = 5$. We can see that the optimum cooling can be achieved near the detuning of $\tilde{\Delta}_q \approx -1.2\omega_m$. It is important to emphasize here that the lowest phonon occupation of the mechanical resonator depends on the device parameters, such as qubit thermal occupation and dissipation rate Γ. For the calculations presented in this section, we assumed the thermal occupation of the qubit and readout cavity to be zero. Another important parameter that affects the ultimate performance of the sideband cooling is sideband parameter ω_m/Γ [53], and cooling to the ground state can only be achieved in sideband-resolved limit $\omega_m/\Gamma \gtrsim 1$.

2.6 Experimental Details

After discussing the performance of the sideband cooling when the qubit is dispersively coupled to the readout cavity, we address the next question on the possibility of the mechanical readout. In the dispersive regime, there is no direct coupling between the cavity and the mechanical resonator. The modulation of qubit frequency translates to the cavity mode via dispersive coupling, and thus creating an effective coupling between the cavity and the mechanical motion. By tuning the transmon qubit frequency near half flux quantum, a large electromechanical coupling with the qubit mode can be obtained. However, when $|\omega_q - \omega_c|$ is large, the effective coupling between the cavity and mechanical mode is suppressed. Next, we show that the addition of cooling tone near the qubit frequency is helpful for the readout of the mechanical motion.

For experimental realization, we use a device consisting of a transmon qubit with a doubly clamped suspended nanowire embedded in the SQUID loop. For the qubit readout, we use a 3D copper rectangular waveguide cavity. The scanning electron microscope (SEM) image of the device is shown in Fig. 8(a). The transmon, fabricated on a silicon substrate coated with highly stressed SiN, is designed to have tunable frequency realized via SQUID. One arm of the SQUID is made suspended to form a nanowire, essentially establishing the mechanical mode. The silicon substrate is placed inside the readout cavity and cool down to 20 mK in a dilution refrigerator. A detailed description of the device fabrication methods and the measurement setup can be found in Ref. [68].

Fig. 8(b) shows the cavity transmission amplitude $|S_{21}|$ as the magnetic flux through the SQUID loop is varied. When the qubit is brought in resonance with the cavity mode, the vacuum-Rabi splitting is observed and two hybrid modes emerge as indicated by the dashed box in Fig. 8(b). From the avoided-crossing, we determine the qubit-cavity coupling strength to be 75 MHz. We measure the dressed cavity frequency to be 6.006 GHz, the maximum qubit frequency to be 7.8 GHz, and the qubit anharmonicity to be -130 MHz. We apply a magnetic field of $B \approx 1.1$ mT, perpendicular to the plane of the SQUID loop. It couples the in-plane motion of the mechanical resonator to the qubit.

To operate in the dispersive limit, we choose a qubit detuning $\Delta = \omega_q - \omega_c$ of $-2\pi\times 900$ MHz. A representative two-tone measurement of the qubit is shown in Fig. 8(c). To record the mechanical motion at this operating point, we apply two tones to the device, a drive tone near the qubit frequency and a probe tone near ω_c and record the mechanical sidebands of the probe tone using a spectrum analyzer. The positioning of various frequencies and drive tones are shown in Fig. 9(a).

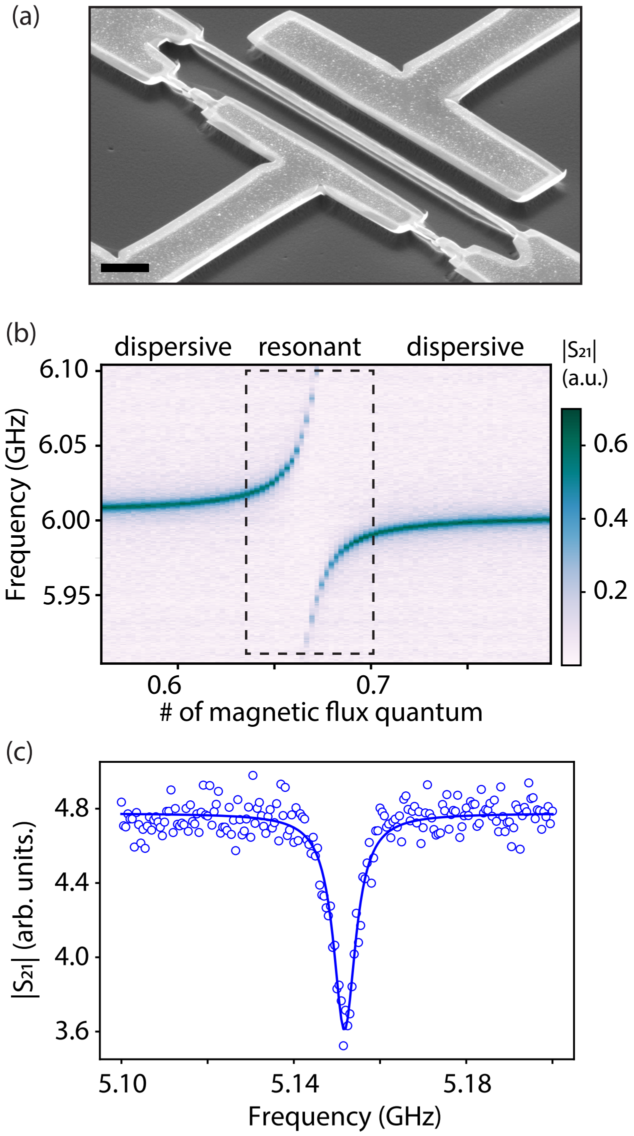

Figure 8: (a) A SEM-image of the device showing the suspended part of the SQUID loop and the Josephson junctions. The length and width of the nanowire is 40 μm and 200 nm, respectively. The scale bar corresponds to 5 μm. (b) Color plot of the cavity transmission $|S_{21}|$ as a function of the magnetic flux through the SQUID loop. (c) Two-tone measurements spectroscopic linewidth of the qubit in the dispersive regime.

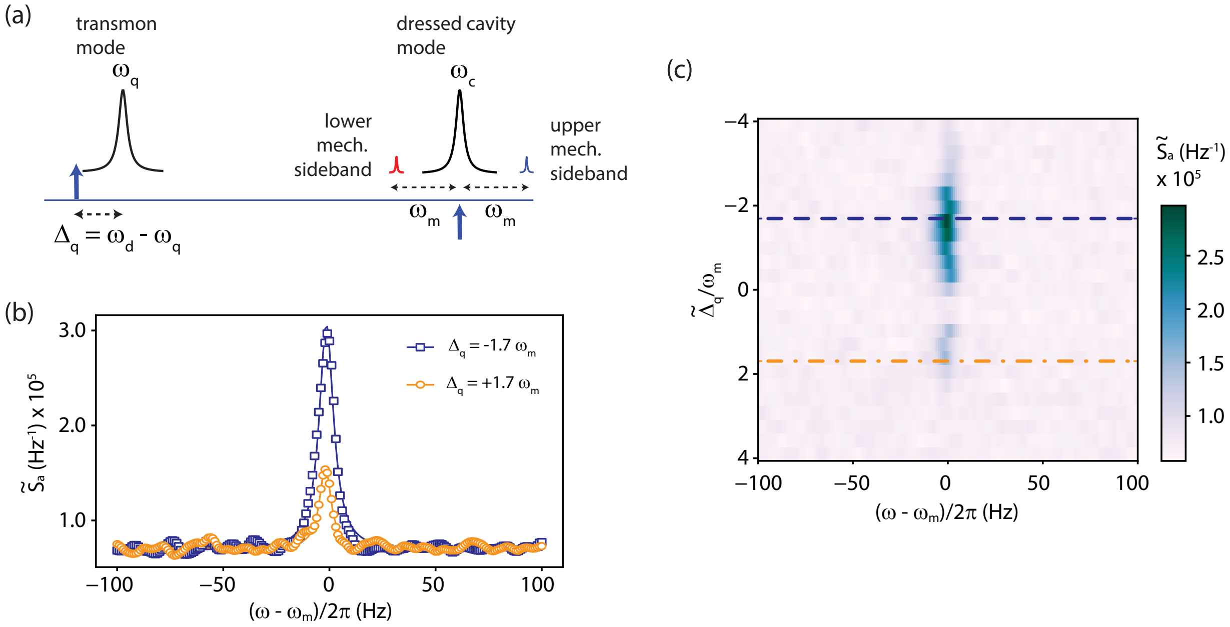

Figure 9: **Experimental Data:** Power spectral density of the cavity mode is measured while varying the drive detuning from the qubit mode. (a) Schematic of the measurement process showing a drive tone present near the qubit mode. The detuning between the qubit and the drive frequency is changed during the measurement. A probe of frequency ω_c is added and its lower and upper mechanical sidebands are recorded with a spectrum analyzer. (b) The spectral density is shown for the drive detuning of $\tilde{\Delta}_q = -1.7\ \omega_m$ (blue square) and $\tilde{\Delta}_q = +1.7\ \omega_m$ (orange circle). The difference in the magnitude of the spectrum as the detuning change sign is evident. The mechanical resonator has a frequency of $\omega_m/2\pi \approx 5.9$ MHz and a linewidth $\gamma_m/2\pi = 6$ Hz. (c) A colorplot of normalized spectral density as a function of detuning and measurement frequency.

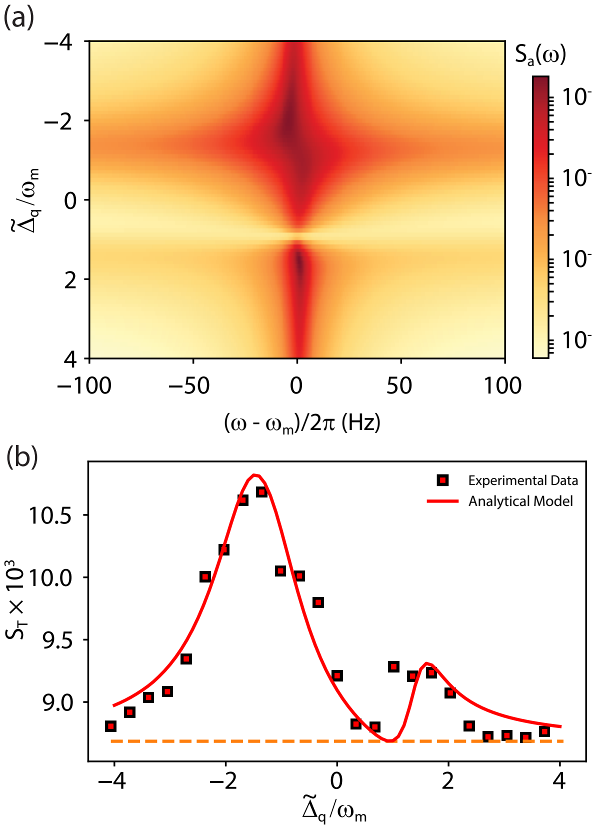

Figure 10: (a) Plot of the calculated cavity mode spectrum from the theoretical model as a function of detuning $\tilde{\Delta}_q$ and frequency. Parameters are taken from the device studied here, as described in the main text. (b) Plot of integrated spectrum $S_T = \int S_a(\omega)d\omega$ for different detuning is calculated from the theoretical and experimental results. The square points indicate the experimental data, plotted as a function of drive detuning ($\tilde{\Delta}_q$). The solid curve is plotted using the estimated device parameters and the analytical expression. The dashed straight line indicates noise level of the measurements. The parameters used for the plots: $\tilde{\Delta}_c = 0$, $\omega_m = 2\pi \times 5.9$ MHz, $J = 2\pi \times 5.6$ MHz, $g = 2\pi \times 3.6$ kHz, $\eta = 2\pi \times 2.8$ MHz, $\kappa = 2\pi \times 4$ MHz, $\Gamma = 2\pi \times 8$ MHz, $\gamma_m = 2\pi \times 6$ Hz, $n_m^i = 350$.

Fig. 9(b) shows the recorded spectrum for two different detunings. The experimentally measured microwave spectrum $S_{mw}(\omega)$ is normalized and represented in the units of intracavity photons defined as, $\tilde{S}_a = S_{mw}(\omega)/(\hbar\omega_c G\kappa_{ex} RBW)$, where G is the estimated net gain of the output line, κ_{ex} is the external coupling rate of the output port of the cavity, and RBW is the resolution bandwidth of the spectrum analyzer. Clearly, the spectrum has a larger peak for negative detuning (blue square) as compared to the one for the positive detuning (orange circle). This asymmetry becomes quite evident as the detuning of qubit drive is varied. Fig. 9(c) shows the colorplot of $\tilde{S}_a$ as drive frequency is varied across the qubit transition.

The mechanical resonator has a frequency of $\omega_m/2\pi \approx 5.9$ MHz and a linewidth of $\gamma_m/2\pi \approx 6$ Hz. Here, we do not observe any backaction on the mechanical resonator. Both, the mechanical frequency and linewidth do not show any measurable change as the detuning $\tilde{\Delta}_q$ is varied across the qubit frequency. This is expected behavior within the experimental parameters. For these measurements, we estimated a single-photon coupling rate of $g_0/2\pi \approx 7.5$ kHz, and measured a qubit linewidth of $\Gamma/2\pi \approx 15$ MHz. The lower sideband parameter and single-photon coupling rate reduces the effect of back-action from the qubit drive.

Another aspect of the measurement is the the enhancement of the transduction and asymmetry with respect to $\tilde{\Delta}_q$. Qualitatively, it can be understood from the qubit-cavity dispersive coupling and the Kerr-term of the qubit mode. A drive tone near the qubit frequency acts like a parametric pump due to the qubit-nonlinearity, resulting in the amplification of the field fluctuations due to electromechanical coupling. Further, due to the dispersive interaction between the qubit and the cavity mode, these field fluctuations result in the modulation of the intracavity probe field, and hence in an improved transduction. The asymmetry in the response is a direct manifestation of the weak anharmonicity of the qubit.

To quantitatively understand the enhancement in the transduction and the asymmetry in spectral density with respect to $\tilde{\Delta}_q$, we compute the cavity spectrum from Eq. 10 as a function of susceptibilities. Approximately, the cavity spectral density can be written as,

$$S_a(\omega) \approx n_m^i \gamma_m (|\chi_m|^2 + |\tilde{\chi}_m|^2)\sigma(\omega), \text{where} \tag{14}$$

$$\sigma(\omega) = \left| \frac{gJ\chi_c\chi_{q\tilde{q}}(\Delta_q - 2\eta)}{\Delta_q + 2i\eta^2\chi_{q\tilde{q}} + g^2\chi_{m\tilde{m}}\chi_{q\tilde{q}}(\Delta_q - 2\eta)} \right|^2 \tag{15}$$

$$\chi_{q\tilde{q}} = \chi_q - \tilde{\chi}_q \tag{16}$$

$$\chi_{m\tilde{m}} = \chi_m - \tilde{\chi}_m. \tag{17}$$

Here, we note that the presence of the effective anharmonicity η in the above equation accounts for the asymmetry observed with respect to the detuning of qubit drive. In the limit $\eta \to 0$, the expression of σ becomes symmetric with respect to Δ_q as it enters the expression through $\chi_{q\tilde{q}}$ only.

Similar to the measurement performed, we analyze the cavity spectral density as $\tilde{\Delta}_q$ is varied. Fig. 10(a) shows theoretically calculated $\tilde{S}_a(\omega)$ using the device parameters. We observe a pattern in $S_a(\omega)$ which is similar to the experimental measurement. For a quantitative comparison, we define the integrated spectrum as $S_T = \int S_a(\omega)d\omega$ and evaluate it for experimental data. Fig. 10(b) shows the plot of S_T from the experimental results shown in Fig. 9(c) and theoretical calculations. A good match validates the approximation made in arriving at the effective Hamiltonian in the theoretical calculations.

2.7 Summary

To summarize, this work has investigated a coupled three-mode hybrid system with a transmon qubit in the presence of external drives. Using the quantum noise and the Lindblad formalism, we study the possibility of sideband cooling of the mechanical resonator by the qubit mode. We find that the readout of the mechanical mode is possible by coupling the transmon qubit to a readout cavity just like in standard c-QED setup while maintaining a dispersive coupling between the cavity and the qubit. In addition, we experimentally demonstrate the applicability of the readout scheme, wherein the experimental results matches closely to the analytical calculations. In this particular experiment, we do not observe any cooling of the mechanical resonator due to lower g_0 and low sideband parameter ($\omega_m/\Gamma \approx\ 0.4$). While the achieved flux responsivity of the qubit in dispersive limit was high 16 GHz/Φ_0, the estimated coupling rate ($g_0/2\pi \approx 7.5$ kHz) was inadequate due to the lower applied magnetic field 1.1 mT.

Looking ahead, the recent experiments have shown promising results for the transmon linewidth in the parallel magnetic field up to hundreds of mT with no significant change in the spectroscopic linewidth [77]. In addition, the flux responsivity of the qubit can be pushed to 40 GHz/Φ_0 by increasing the maximum qubit frequency. With these parameters, the single-photon electromechanical coupling between qubit and mechanical resonator can be enhanced up to 10 MHz, bringing the system near to ultra-strong coupling regime [78]. Such regime opens up the possibilities of observing the photon blockade effects [51], non-trivial ground state [32] and a path of using low frequency mechanical resonator in the quantum technologies.

3 Progress report: January 2022 - January 2023

3.1 Executive summary

With artificially engineered systems, it is now possible to realize the coherent interaction rate, which can become comparable to the mode frequencies, a regime known as ultrastrong coupling (USC). We experimentally realize a cavity-electromechanical device using a superconducting waveguide cavity and a mechanical resonator. In the presence of a strong pump, the mechanical-polaritons splitting can nearly reach 81% of the mechanical frequency, overwhelming all the dissipation rates. Beyond the USC limit, the steady-state response becomes unstable. We systematically measure the boundary of the unstable response while varying the pump parameters. The unstable dynamics display rich phases, such as self-induced oscillations, period-doubling bifurcation, period-tripling oscillations, and ultimately leading to the chaotic behaviour. The experimental results and their theoretical modelling suggest the importance of residual nonlinear interaction terms in the weak-dissipative regime.

3.2 Introduction

Radiation-pressure interaction is fundamental to the cavity-optomechanical systems consisting of a mechanical mode coupled to an electromagnetic mode (EM) [44]. With technological advancements, cavity optomechanical devices have been successful in controlling the low-frequency mechanical mode down to their quantum regime [43]. Several demonstrations pertaining to the quantum state preparation [45, 46, 50, 79] and entanglement [80, 81, 48, 49], signal transduction [82, 83, 84], and topological physics using the mechanical modes have been shown [85, 86].

The coherent coupling rate characterizing the interaction between the EM mode (ω_c) and the mechanical mode (ω_m), is a key figure of merit in such devices [44, 43]. The energy dissipation rates of the two modes (κ, γ_m) capture the incoherent coupling with their thermal baths. Based on the relative strengths of these rates, several interesting scenarios are feasible. When the coherent coupling rate (g) exceeds the dissipative coupling rates of the two modes ($g \gg \kappa, \gamma_m$), the two modes hybridize, resulting in new eigenstates [87, 88]. Further, when the coherent coupling rate becomes a significant fraction of the mode frequencies, the composite system enters the "ultrastrong coupling" (USC) limit [89]. In this limit, the two modes hybridize in a non-trivial way leading to an entangled ground state in the quantum regime [90, 91]. The USC limit has been experimentally demonstrated in several systems where two modes interact nearly resonantly [78, 92].

In cavity optomechanical systems, however, the EM mode and mechanical mode interact dispersively ($\omega_c \gg \omega_m$). The nonlinear radiation-pressure interaction can be described by $H_i/\hbar = g_0 a^\dagger a(b+b^\dagger)$, where g_0 is the single-photon coupling strength and $a(b)$'s are the ladder operators for the cavity(mechanical) mode. In the presence of a strong coherent pump, the interaction Hamiltonian can be linearized to $H_i/\hbar \simeq g(a + a^\dagger)(b + b^\dagger)$, where $g = g_0\sqrt{n_d}$ is the parametric coupling rate and n_d is the number of the pump photons in the cavity. With the ability to control the parametric coupling rate, several regimes, such as quantum coherent coupling, and steady-state quantum entanglement between the

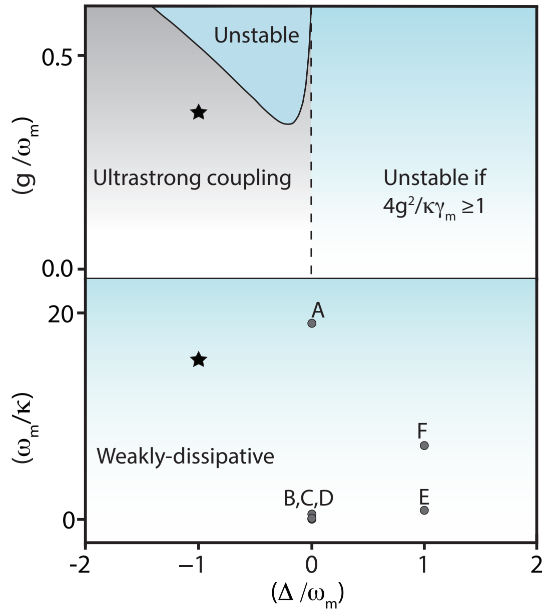

Figure 11: Top panel shows the schematic of the parameter space of a cavity-electromechanical s ystem in the steady state. The gray-color gradient represents the ultrastrong coupling (USC) regime. The cyan color marks the unstable region. The bottom panel compares the sideband-resolution parameter of this study (marked by $\star$) and the earlier studies on instabilities. The data points A to F are from refs [100, 103, 104, 101, 102, 105], respectively.

two modes can be reached [88, 93, 49]. Ultimately, due to the nonlinear nature of the radiation-pressure interaction, the response becomes unstable as shown schematically in Fig. 11.

Indeed, various phenomena in the unstable region such as limit cycle, period doubling bifurcations, and chaos have been extensively studied [94, 95, 96, 97, 98]. Experimentally, these effects have been primarily explored in the strong dissipative regime ($\omega_m \lesssim \kappa$) or with the blue-detuned pump [99, 100, 101, 102, 103, 104, 105] (see Fig. 11). The instabilities near the ultrastrong coupling limit, however, allow to explore the nonlinear dynamics of the cavity optomechanical system in the *weakly dissipative* limit ($\gamma_m, \kappa \ll 2g \lesssim \omega_m$). The nonlinear dynamics with weak dissipation is unique and is predicted to show transient chaos, quasi-periodic route to chaos and lower threshold powers for the onset of chaos [106, 107].

3.3 Technical Details and results

We use a cavity electromechanical device in the microwave domain to probe the route to chaos when it is operated into the USC limit. We first demonstrate the USC by performing the spectroscopic and time-domain measurements. We probe the stability of the device when the pump detuning near the red-sideband and injected power are varied. The unstable region shows very rich phases in the parameter space, such as the self-induced oscillation, period-doubling bifurcations, period-tripling oscillations, and chaotic behaviour [96, 106, 107]. We find that the measured threshold powers for the onset of instabilities are lower than the ones predicted from a nonlinear model considering the optomechanical interaction and a Kerr-term in the cavity.

We use the three-dimensional cavity-based platform to realize the cavity-electromechanical device [29, 30, 31]. The waveguide cavity-based electromechanical device offers a higher dynamic range for the pumped photons, which is highly desirable to reach the USC limit [31, 32]. As shown in Fig. 14(a,b), the device consists of a rectangular waveguide cavity, and a drumhead-shaped mechanical resonator in the form of a parallel plate capacitor patterned on a sapphire chip. The patterned sapphire chip is placed at the center of the cavity. The electrical pads to the drumhead are then directly wire-bonded to the cavity walls to integrate with the cavity mode [31].

3.4 Device fabrication

The nanofabrication consists of several steps, which are described below. The details of the fabrication processes are schematically illustrated in the Fig. 12. We begin with a 2-inch diameter double-side polished sapphire wafer and dice it into smaller substrates of 5×8 mm^2 size. Aluminium parallel plate capacitors are then fabricated onto these substrates after cleaning.

Step-1 Substrate cleaning: These diced pieces are heated on a sample holder in PG remover for 30 minutes at 80°C and then rinsed with IPA. Samples are then dipped in concentrated HNO_3 for 10 minutes and followed by rinsing with DI water. The samples are then cleaned in piranha solution for 10 minutes, followed by rinsing with DI water.

Step-2 Patterning of the base electrode: Cleaned wafer pieces are loaded in an electron beam evaporator, and then 60 nm thin film of aluminium is deposited with a deposition rate of 3 Å/s. Subsequently, the samples are spin-coated with photoresist (S1813). We use a spin speed of 6000 RPM to minimise the edge bead. The resist-coated samples are baked at 110°C for 90 sec. The base electrode is patterned using a MJB4 lithography tool, followed by development in a 4:1 solution of water and developer AZ351B for 6-7 seconds. The exposed Al is etched with a 3:1 solution of H_3PO_4 and HNO_3 and rinsed with DI water. The samples are dipped in a 1:2 solution of MF26A and water for 10 seconds to remove the Al oxide layer, followed by rinsing with DI water. Removal of the photoresist is done in acetone for 5 minutes, followed by rinsing with IPA. Further, the samples are exposed to O_2 plasma with 50 W power for 1 minute to remove any residue of photoresist.

Step-3 Patterning of the sacrificial layer: Silicon of 200 nm is deposited using a sputtering machine followed by spin coating with photoresist AZ5214E at 6000 RPM and followed by baking for 90 seconds at 110°C. Similar to previous steps, the sacrificial layer is patterned with MJB4 and developed in a 4:1 solution of water and AZ351B for 10-12 seconds. The exposed silicon is etched in a reactive ion etching machine with SF_6 gas for 2 minutes, followed by photoresist removal in 80°C hot PG remover for 30 minutes. The sample is again exposed to O_2 plasma with 50 W power for 2 minutes to remove any residue of photoresist.

Step-4 Patterning of the top electrode: A 100 nm thick film is deposited on the

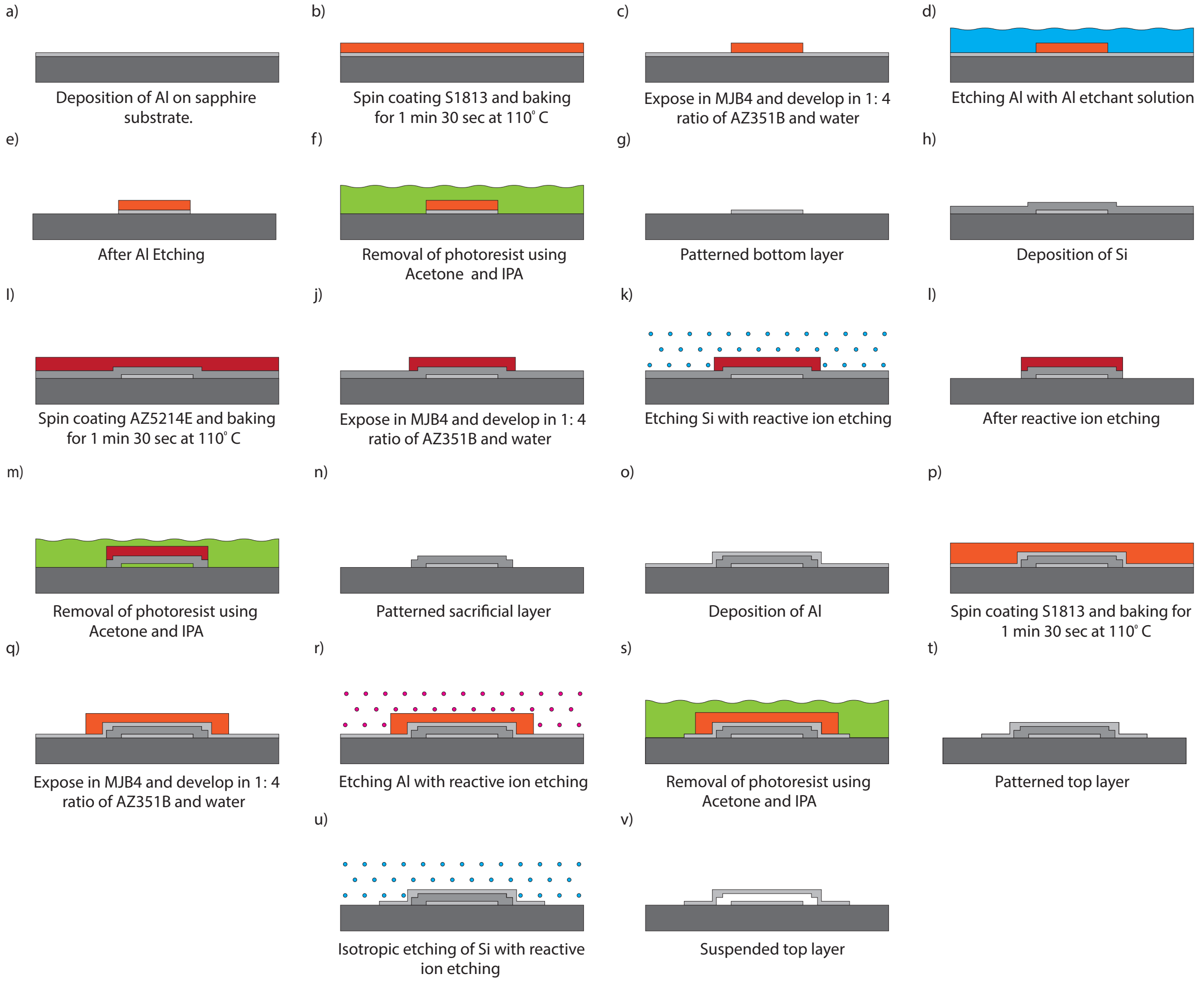

a) Deposition of Al on sapphire substrate.

b) Spin coating S1813 and baking for 1 min 30 sec at 110° C

c) Expose in MJB4 and develop in 1: 4 ratio of AZ351B and water

d) Etching Al with Al etchant solution

e) After Al Etching

f) Removal of photoresist using Acetone and IPA

g) Patterned bottom layer

h) Deposition of Si

l) Spin coating AZ5214E and baking for 1 min 30 sec at 110° C

j) Expose in MJB4 and develop in 1: 4 ratio of AZ351B and water

k) Etching Si with reactive ion etching

l) After reactive ion etching

m) Removal of photoresist using Acetone and IPA

n) Patterned sacrificial layer

o) Deposition of Al

p) Spin coating S1813 and baking for 1 min 30 sec at 110° C

q) Expose in MJB4 and develop in 1: 4 ratio of AZ351B and water

r) Etching Al with reactive ion etching

s) Removal of photoresist using Acetone and IPA

t) Patterned top layer

u) Isotropic etching of Si with reactive ion etching

v) Suspended top layer

Figure 12: A schematic of the fabrication process summarizing the key steps

samples using the sputtering technique. Patterning of the top electrode follows the exact same procedure as the bottom electrode.

Step-5 Etching of the sacrificial layer and release of the drum: To avoid any electrostatic effect leading to the collapse of the drum, we shorted the two electrodes of the sample using a wire bond before the release process. The Si-sacrificial layer is etched using a high-pressure SF_6 etch in a reactive ion system. The following are the typical RIE etch parameters: 50W RF power, 95 mTorr chamber pressure, 100 sccm flow rate of SF_6, seven cycles of 8 mins of etching process with 2 mins break between each cycle.

3.5 Measurement setup

Fig. 13(a) shows the measurement set up for the optomechanically induced absorption technique. We use a red detuned strong pump generated by a signal generator (R&S - SMF100A) and a probe tone near the cavity resonance frequency provided by a vector network analyser (R&S - ZNB20). The time base of both the signal generators are

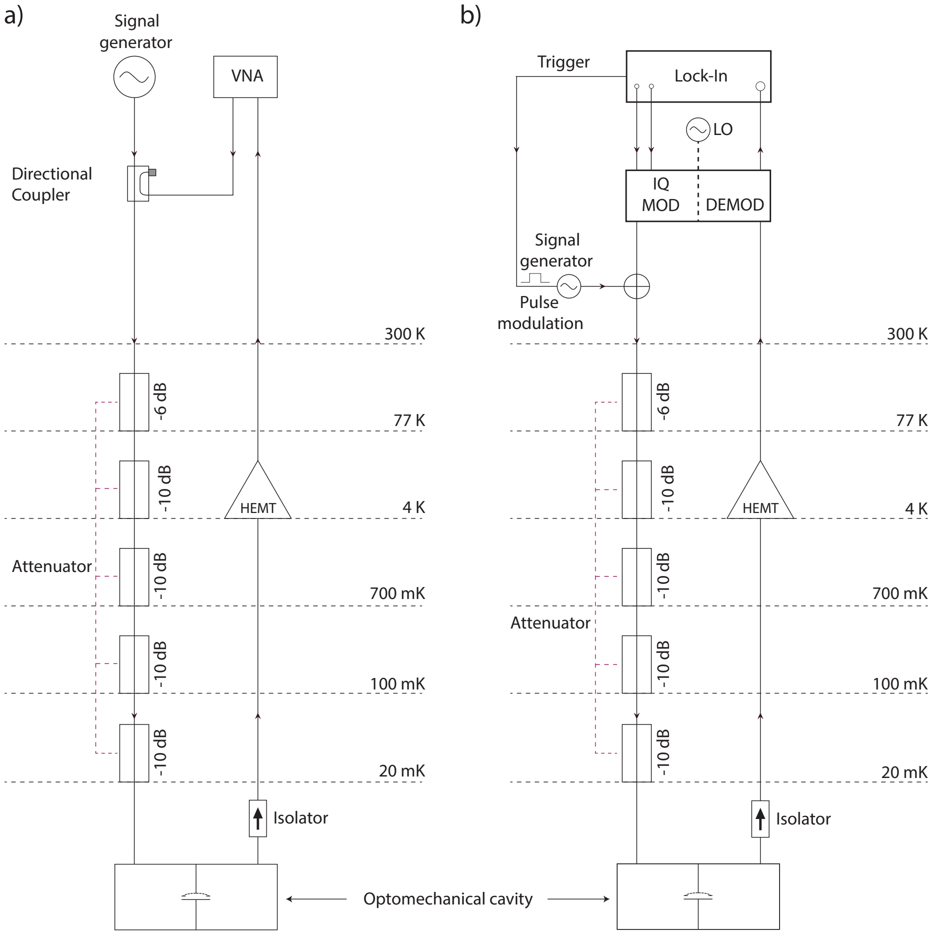

Figure 13: Setup for (a) spectroscopy and (b) time-domain measurements.

synchronized by an external 10 MHz clock. We use a directional coupler at the input to combine both the signals. The input signal goes through a series of attenuators at different cooling stages in the dilution refrigerator before reaching the input of the cavity. The output from the cavity gets amplified by a HEMT amplifier at the 4 K stage before reaching the input of the vector network analyser.

Fig. 13(b) shows the time domain measurement setup used to perform the optomechanical swap. The pump is pulse-modulated using a trigger. The pulse-modulated pump output is then added to the probe signal. To maintain vector control over the probe signal, we use a home-built IQ-modulation-demodulation box based on IQ-mixer (Marki-IQ4509) for up-conversion, and a Mini-Circuits-ZMX-10G+ three-port mixer for down-conversion. The base-band signals for the probe are generated from the 2-channel outputs of a lock-in amplifier (Zurich instruments - UHFLI). The demodulated RF output from the demodulator box is sent to the lock-in amplifier's inputs to record the quadratures $I(t)$ and $Q(t)$.

The sample-mounted cavity is cooled down to 20 mK in a dilution fridge. Fig. 14(c) shows the measurement of the cavity transmission at the base temperature. The bare cavity is designed to have the fundamental resonant mode frequency of 7.5 GHz. How-

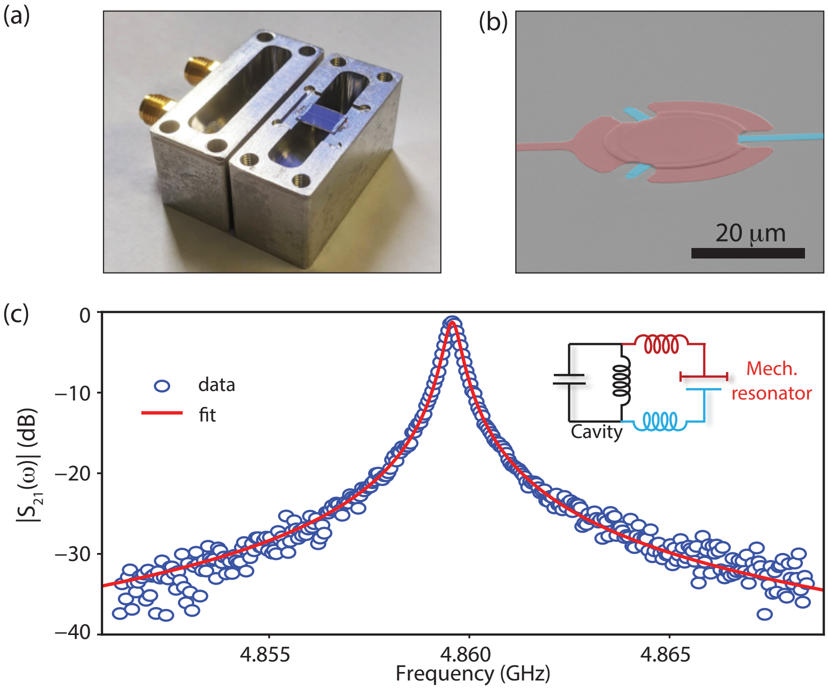

Figure 14: a) Image of the waveguide cavity along with a patterned mechanical resonator on the sapphire chip. The cavity has dimensions of $26 \times 26 \times 6$ mm^3. b) False color image of the mechanical resonator forming a parallel plate capacitor with another plate on the substrate. The separation between the capacitor plates at room temperature is approximately 200 nm. The capacitor leads are connected to the cavity walls via multiple wirebonds to the electrodes. c) Measurement of the transmission coefficient $|S_{21}|$ of the device at the base temperature. The inset shows the equivalent circuit diagram of the cavity electromechanical device.

ever, the electromechanical capacitor perturbs the mode shape significantly, and lowers the mode frequency to $\omega_c/2\pi \approx 4.86$ GHz. The reduction in the resonant frequency of the cavity results from the electromechanical capacitance and the inductance of the connecting electrodes introduced after the addition of a patterned sapphire chip. We measure the input, output, and the internal dissipation rates of $\kappa_{e1}/2\pi \approx 90$ kHz, $\kappa_{e2}/2\pi \approx 190$ kHz, and $\kappa_i/2\pi \approx 100$ kHz, respectively. At low temperatures, we estimated that the gap between the electromechanical capacitor plates reduces to approx. 32 nm due to thermal contraction [47, 108], which helps in achieving a single photon coupling rate $g_0/2\pi$ of 165 Hz.

3.6 Demonstration of the ultrastrong coupling regime

We measure the transmission coefficient $|S_{21}(\omega)|$ through the cavity using a weak probe tone while injecting a pump detuned near the red sideband $\omega_c - \omega_m$. At relatively lower pump powers, the optomechanically induced absorption (OMIA) setup allows us to determine the mechanical frequency $\omega_m/2\pi \approx 6.32$ MHz [109]. At relatively higher pump powers, the response turns into two well-separated peaks confirming the new eigenmodes of the system as shown in Fig. 18(a). The peak separation being $0.81\omega_m$ marks the ultra-

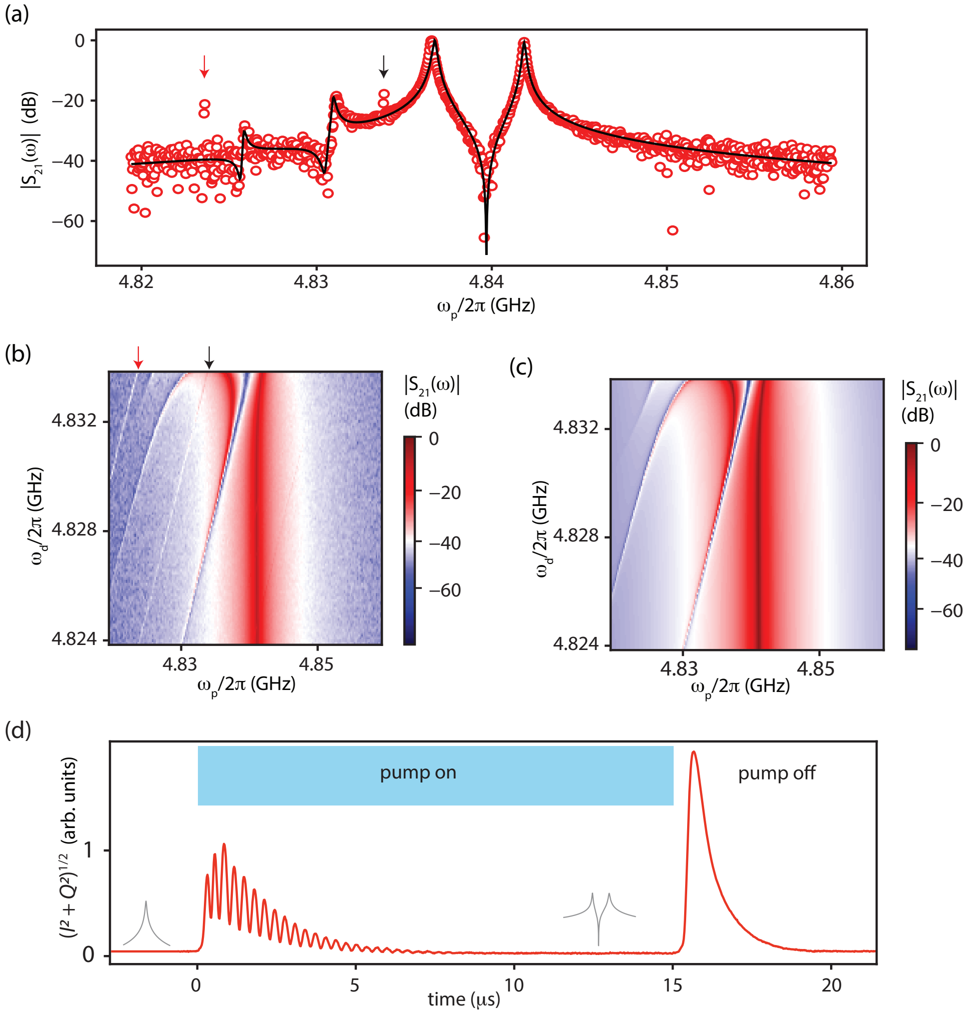

Figure 15: **Demonstration of the ultrastrong coupling:** (a) The normalized magnitude of the cavity transmission $|S_{21}(\omega)|$ (red-circles) while applying a strong pump near the red-sideband. The black line shows the calculated $|S_{21}(\omega)|$ while including the static Kerr shift of the cavity. (b) The colorplot of measured $|S_{21}(\omega)|$ as the pump frequency ω_d is varied at a fixed pump power. The black arrow shows the position of the pump signal, while the red arrow indicated another weakly coupled mechanical mode. (c) Colorplot of $|S_{21}(\omega)|$ obtained from the calculations. (d) Measurement of the transmission amplitude in the time domain while modulating the interaction strength. The pump frequency is set near the lower mechanical sideband. A weak probe signal near ω_c is used to measure the cavity transmission continuously. The gray curves represent the steady-state cavity transmission $|S_{21}(\omega)|$ in the frequency domain.

strong coupling between the mechanical resonator and the cavity. The transmission measurement shows the presence of an additional weakly coupled mechanical mode, indicated by the red arrow. Two more features arising from the interference of the down-scattered pump signal and the probe signal can be seen. Fig. 18(b) shows the measurement of $|S_{21}|$ as the frequency of the pump is varied while maintaining a constant power at the signal generator.

The presence of a strong intracavity pump-field leads to a static shift of the equilibrium position of the mechanical resonator, given by $x_s = (2g_0 n_d/\omega_m)x_{zp}$, where x_{zp} is the zero-point motion of the mechanical resonator. The shift in the equilibrium position of the mechanical resonator leads to a Kerr shift of the cavity frequency by $-2g_0^2 n_d/\omega_m$. The total shift in the cavity frequency comes from the static nature of the radiation-pressure force and non-linear kinetic inductance of the superconducting film. We emphasize here that at high pump powers, the Kerr shift of the cavity becomes significant, and it must be considered to capture the cavity transmission faithfully. In this case, we found a cavity shift of $\sim$1.76 MHz at the maximum pump power used in the experiment. It corresponds to an optomechanical Kerr coefficient of 8.6 mHz/photon and a kinetic inductance Kerr coefficient of approx. 5 mHz/photon at the maximum pump power.

To theoretically model the cavity transmission, we expand the interaction Hamiltonian, H_i around the mean field of the pump and obtain the quantum-Langevin equations of motion. Without using the rotating-wave approximation and by retaining the static Kerr shift of the cavity frequency, the steady-state response can be obtained from the inverse of the mode-coupling matrix. The solid line in Fig. 18(a) and colorplot in Fig. 18(c) show the calculated transmission coefficient using the experimentally determined device parameters. While in general, additional weakly coupled mechanical modes can also be included in the calculations, we neglect them here for simplicity.

The onset of the strong-coupling, allows a coherent swap of the excitations between the cavity and the mechanical mode. It thus enables the high-speed optomechanical swap gates in the ultrastrong coupling limit. To explore the maximum speed of the optomechanical swap, we perform time domain measurements in this limit. We modulate the interaction strength $g(t)$, which is controlled by the amplitude of the pump tone. The transmission through the cavity is monitored by applying a weak continuous probe signal near ω_c. To demodulate the probe signal, we first mix it down using an external mixer and then sending it to a high-speed lock-in amplifier to further demodulate the quadratures with a short integration time (100 ns).

Fig. 18(d) shows the measurement of the magnitude of the demodulated signals $(I(t), Q(t))$ as the interaction strength $g(t)$ is modulated. For this measurement, the interaction strength is modulated to 1.55 MHz. The probe frequency is detuned from the cavity resonant frequency by $(\omega_p - \omega_c)/2\pi = 372$ kHz. Therefore, the transmission is small even when the pump tone is off ($t < 0$). In the steady-state when the pump is turned on ($t \approx 10$ μs), the transmission is low again due to the formation of mechanical-polariton modes. Due to the strong static Kerr shift of the cavity, the probe tone appears approximately to the center of splitted peaks, and therefore results in a low transmission.

When interaction is just switched on, the transient response shows the oscillations arising from the coherent energy exchange between the mechanical and the cavity modes.

Table 2: Key device parameters

Description	Parameter	Value	Unit
Cavity frequency	ω_c	4.86	GHz
Microwave input coupling rate	κ_{e1}	90	kHz
Microwave output coupling rate	κ_{e2}	190	kHz
Cavity linewidth	κ	380	kHz
Mechanical frequency	ω_m	6.32	MHz
Mechanical dissipation rate	γ_m	20	Hz
Single photon coupling rate	g_0	165	Hz

The oscillation frequency of 3.1 MHz corresponds to the characteristic swap time of 160 ns. The amplitude of the oscillations decays at a rate $\simeq \kappa/4$ set by joint dissipation of the two polaritons. When the pump is turned off, the energy stored in the two polariton modes reemerges near the probe frequency, and the amplitude decays at $\kappa/2$. It might be important to remark here that as we operate in the sideband-resolved limit ($\omega_m/\kappa = 16.5$), the probe and pump microwave fields do not spectrally overlap despite a sharp pulse modulation of the input pump field.

3.7 Key device parameters

Table 2 lists some key device parameters extracted from various experiments. Calibration of the external coupling rates of the microwave input and output ports (κ_{e1} and κ_{e2}) is performed in a separate cooldown where we measured the reflection coefficients from both microwave ports using two separate HEMT amplifiers.

3.8 Parametic instabilities near ultrastrong coupling

After establishing the USC in the present experiment, we now discuss the parametric instabilities arising at the high pump powers. At the core of it, the instabilities stem from the nonlinear interaction between the microwave field and the mechanical motion. To experimentally investigate the phase space of the parametric instabilities and their nature, we measure the microwave power spectral density (PSD) using a spectrum analyzer while varying the pump power P_i and pump detuning $\Delta = (\omega_d - \omega_c)$. As P_i is increased, the self-induced oscillations appear as multiple peaks separated by ω_m in the microwave PSD. Fig. 16(a) shows the PSD of different kinds of responses. The first (top) panel corresponds to the instability due to the self-induced oscillations where the peaks are separated by ω_m. The second panel corresponds to the 1^{st} period-doubling bifurcations (PDB), where the peaks are separated by $\omega_m/2$. The third panel shows the period-tripled oscillations where the peaks are separated by $\omega_m/3$. The fourth panel shows the response where the power is uniformly distributed over a broad range of frequency, corresponding to the chaotic response. These different phases of unstable response are summarized in Fig. 16(b). The gray-color region represents the parametrically unstable response. The boundary of the gray region marks the threshold power for the self-induced oscillations. With decrease in Δ, the circulating power in the cavity decreases, and the threshold power for the onset

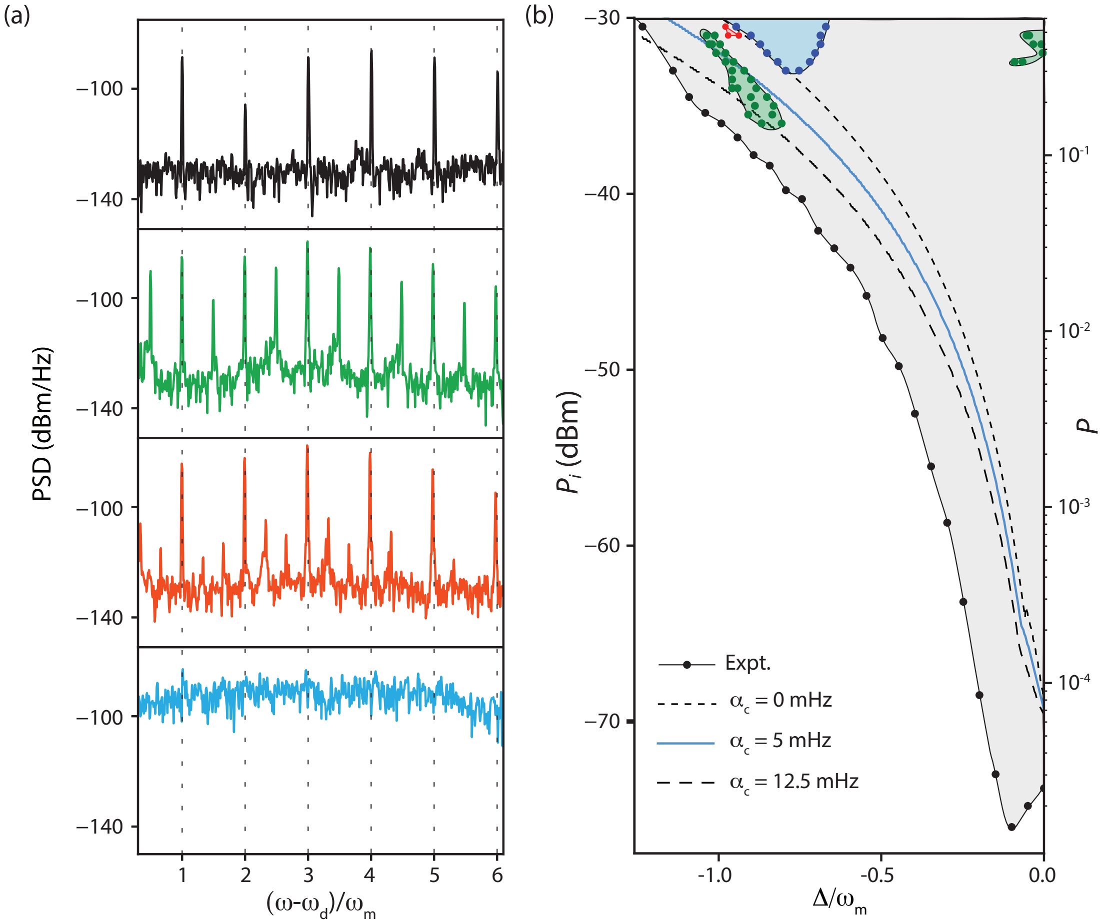

Figure 16: **Instabilities near the ultrastrong coupling:** (a) Measurement of the single sideband microwave power spectral density (PSD) for different injected pump powers P_i. The panels from top to bottom show the self-induced oscillations, first period-doubling bifurcations, period tripling oscillations, and the chaotic behaviour. (b) The gray region represents the boundary of self-induced oscillations. The black circles are the experimentally measured points. At higher injected pump powers, the region of period-doubling bifurcations is represented by the green region. The period tripled oscillations are shown by the red-colored region. The region of chaotic behaviour is shown by the cyan-colored region. Experimentally measured points are shown by the circles of different colors. The solid blue line and the dashed lines show the unstable boundary obtained from the theoretical calculation.

of the instability increases. The regions of 1^{st}-PDB, period tripled oscillations and chaos are color-coded within the unstable region.

To understand these results, we use the classical nonlinear dynamics approach. We start with the full cavity optomechanical Hamiltonian *i.e.* $H_i/\hbar = g_0\hat{a}^\dagger\hat{a}(\hat{b} + \hat{b}^\dagger)$. In addition, motivated by the observation of period-tripling oscillations and the relevance of the kinetic inductance at the high pump powers, we include a weak nonlinear term in the cavity Hamiltonian, given by $-(\alpha_c/2)(\hat{a}^\dagger\hat{a})^2$. Using the semi-classical approximation, we obtain the classical equations of motion (EOM) for the cavity and the mechanical quadratures. From EOMs, we find the fixed points and perform a linear stability test, which is similar to the Routh-Hurwitz criteria, *i.e.* the solutions are stable iff all the eigenvalues of the evolution matrix of small perturbations around the fixed points have a negative real part [110]. The detailed calculations are summarized in the next section.

3.9 Calculations of the cavity transmission

The Hamiltonian for an optomechanical cavity system is given by

$$\tilde{\mathcal{H}} = \hbar\omega_c(\hat{x})(\hat{n} + 1/2) + \hbar\omega_m(b^\dagger b + 1/2), \tag{18}$$

where the operator $b(b^\dagger)$ is the annihilation(creation) operator for the mechanical resonator, and $\omega_c(\omega_m)$ represents the resonant frequency of the microwave cavity (mechanical resonator). The operator $\hat{n}$ is the photon number operator for the microwave cavity. The resonant frequency of the microwave cavity depends on the gap between the capacitor plates. As the bottom plate is fixed, the microwave cavity's resonant frequency depends on the top plate's position (mechanical oscillator), which is freely suspended. When the amplitude of the mechanical oscillator is small, we can expand $\omega_c(\hat{x}) \simeq \omega_c - g_0\hat{x}/x_{zp}$, where $x_{zp} = \sqrt{\hbar/2m\omega_m}$ is the vacuum fluctuations of the mechanical oscillator, g_0 is the single photon coupling strength, and m is the mass of the mechanical resonator.

With a pump tone at $\omega_d = \omega_c + \Delta$, the cavity gets populated with n_d coherent microwave photons with the pump tone frequency. The number of photons inside the cavity after writing in terms of mean coherent amplitude $\sqrt{n_d}$ and fluctuating term $\hat{a}$ becomes

$$\hat{n} = (\sqrt{n_d}e^{i\omega_d t} + \hat{a}^\dagger)(\sqrt{n_d}e^{-i\omega_d t} + \hat{a}) = n_d + \sqrt{n_d}(\hat{a}^\dagger e^{-i\omega_d t} + \hat{a}e^{i\omega_d t}) + a^\dagger a. \tag{19}$$

Thus, the resultant Hamiltonian can be written as,

$$\tilde{\mathcal{H}} = \hbar\omega_c n_d + \hbar\omega_c\hat{a}^\dagger\hat{a} + \hbar\omega_c\sqrt{n_d}(\hat{a}e^{i\omega_d t} + \hat{a}^\dagger e^{-i\omega_d t}) - \hbar g_0 n_d(\hat{b}^\dagger + \hat{b}) +$$
$$\hbar g(\hat{a}^\dagger e^{-i\omega_d t} + \hat{a}e^{i\omega_d t})(\hat{b}^\dagger + \hat{b}) + \frac{\hbar}{2}g_0(\hat{b}^\dagger + \hat{b}) - \hbar g_0(\hat{b}^\dagger + \hat{b})\hat{a}^\dagger\hat{a} + \hbar\omega_m\hat{b}^\dagger\hat{b}.$$

To get the equation of motion for the coupled system, we use the Heisenberg-Langevin approach to get

$$\dot{\hat{a}} = -\frac{\kappa}{2}\hat{a} + \sqrt{\kappa_{e1}}\hat{a}_{in} - i\omega_c\sqrt{n_d}e^{-i\omega_d t} + ig_0(\hat{b}^\dagger + \hat{b})\hat{a} + ig(\hat{b}^\dagger + \hat{b})e^{-i\omega_d t} - i\omega_c\hat{a}, \tag{20}$$

$$\dot{\hat{b}} = (-i\omega_m - \frac{\gamma_m}{2})b + ig_0\hat{a}^\dagger\hat{a} + \sqrt{\gamma_m}\hat{b}_{in} + ig_0 n_d + i\sqrt{n_d}g_0(\hat{a}e^{-i\omega_d t} + \hat{a}^\dagger e^{-i\omega_d t}), \tag{21}$$

where κ_{e1} is the external coupling rate of the cavity, γ is the mechanical dissipation rate, and $\hat{a}_{in}(\hat{b}_{in})$ is the input noise operators for the microwave (mechanical) field.

Taking the Fourier transform of the equation of motions and putting them in a compact matrix form, we get

$$C(\omega)\begin{bmatrix}\hat{a}(\omega+\omega_d)\\ \hat{b}(\omega)\\ \hat{a}^\dagger(\omega_d-\omega)\\ \hat{b}^\dagger(-\omega)\end{bmatrix} + \begin{bmatrix}-\omega_c\sqrt{n_d}\delta(\omega)\\ g_0 n_d\delta(\omega)\\ \omega_c\sqrt{n_d}\delta(\omega)\\ -g_0 n_d\delta(\omega)\end{bmatrix} = \begin{bmatrix}i\sqrt{\kappa_{e1}}\hat{a}_{in}(\omega+\omega_d)\\ i\sqrt{\gamma_m}\hat{b}_{in}(\omega)\\ i\sqrt{\kappa_{e1}}\hat{a}_{in}^\dagger(\omega_d-\omega)\\ i\sqrt{\gamma_m}\hat{b}_{in}^\dagger(-\omega)\end{bmatrix}. \tag{22}$$

The mode-coupling matrix $C(\omega)$ is given by

$$C(\omega) = \begin{bmatrix}{\chi_a}^{-1}(\omega+\omega_d) & g & 0 & g\\ g & {\chi_b}^{-1}(\omega) & g & 0\\ 0 & -g & -{\chi_a}^{-1}(\omega_d-\omega)^* & -g\\ -g & 0 & -g & -{\chi_b}^{-1}(-\omega)^*\end{bmatrix}, \tag{23}$$

where

$$\chi_a(\omega) = 1/(\omega - \omega_c + i\kappa/2), \tag{24}$$

$$\chi_b(\omega) = 1/(\omega - \omega_m + i\gamma_m/2) \tag{25}$$

are the complex susceptibility functions for the cavity and mechanical mode, respectively.

We use optomechanically induced absorption (OMIA) to couple the cavity and mechanical motion and get the resultant response of the dressed mode. Here, we provide a strong red-detuned pump at a frequency $\omega_c - \omega_m$ and a weak probe tone near cavity resonance frequency, ω_c. The resultant transmission through the cavity at a frequency ω is then given by

$$T(\omega) = i\sqrt{\kappa_{e1}\kappa_{e2}}\chi_a^{eff}(\omega), \tag{26}$$

where $\chi_a^{eff}(\omega)$ is given by $(C^{-1}(\omega))_{11}$, $\kappa_{e1}(\kappa_{e2})$ is the input(output) coupling rate.

3.10 Linear Stability test (Routh-Hurwitz stability criteria)

To understand the instabilities at large pump powers, we consider the optomechanical Kerr-nonlinearity and the kinetic inductance of aluminium film. We start with the full optomechanical Hamiltonian in the rotating frame of the pump frequency. It can be written as,

$$\mathcal{H} = -\Delta\hat{a}^\dagger\hat{a} - \frac{\alpha_c}{2}\hat{a}^\dagger\hat{a}^\dagger\hat{a}\hat{a} + \omega_m\hat{b}^\dagger\hat{b} - g_0\hat{a}^\dagger\hat{a}(\hat{b}+\hat{b}^\dagger) + iE(\hat{a}+\hat{a}^\dagger), \tag{27}$$

where α_c is the Kerr-coefficient to model the kinetic inductance. Using the Heisenberg-Langevin approach and the semi-classical approximation, the equations of motions can be written as,

$$\dot{\alpha} = (i\Delta - \frac{\kappa}{2})\alpha + i\alpha_c\left|\alpha\right|^2\alpha + ig_0\alpha(\beta+\beta^*) + E, \tag{28}$$

$$\dot{\beta} = -(i\omega_m + \frac{\gamma_m}{2})\beta + ig_0 \left|\alpha\right|^2, \tag{29}$$

where $E = \sqrt{\kappa_{e1}}\ \hat{a}_{in}$, $\alpha = \langle\hat{a}\rangle$ and $\beta = \langle\hat{b}\rangle$. By representing α and β in the complex form, we get

$$\alpha = x + iy, \tag{30}$$

$$\beta = p + iq. \tag{31}$$

Therefore,

$$\dot{x} = f_1(x, y, p, q) = -\frac{\kappa}{2}x - \Delta y - 2g_0 py - \alpha_c y(x^2 + y^2) + E, \tag{32}$$

$$\dot{y} = f_2(x, y, p, q) = \Delta x - \frac{\kappa}{2}y + 2g_0 px + \alpha_c x(x^2 + y^2), \tag{33}$$

$$\dot{p} = f_3(x, y, p, q) = -\frac{\gamma_m}{2}p + \omega_m q, \tag{34}$$

$$\dot{q} = f_4(x, y, p, q) = g_0 x^2 + g_0 y^2 - \omega_m p - \frac{\gamma_m}{2}q. \tag{35}$$

Following the approach used in Ref. [96, 107], we obtain the fixed points of the system by setting the first derivative of the real and imaginary parts of both α and β to zero, *i.e.* $\dot{x} = \dot{y} = \dot{p} = \dot{q} = 0$. Combining Eq. 32 and Eq. 33 and representing x, y, q in terms of p, we get

$$x = \frac{\kappa}{2}\frac{E}{A^2 + (\frac{\kappa}{2})^2}, \tag{36}$$

$$y = \frac{A\ E}{A^2 + (\frac{\kappa}{2})^2}, \tag{37}$$

$$q = \frac{\gamma_m}{2\omega_m}p, \tag{38}$$

where

$$A = \Delta + B\ p \tag{39}$$

and

$$B = \left[2g_0 + \frac{\alpha_c}{g_0}(\omega_m + \frac{\gamma_m^2}{4\omega_m})\right]. \tag{40}$$

Substituting the above calculated values of x, y, q in Eq. 35, we get a cubic polynomial equation,

$$B^2\left(\omega_m + \frac{\gamma_m^2}{4\omega_m}\right)p^3 + 2B\Delta\left(\omega_m + \frac{\gamma_m^2}{4\omega_m}\right)\ p^2 + \left(\Delta^2 + \frac{\kappa^2}{4}\right)\left(\omega_m + \frac{\gamma_m^2}{4\omega_m}\right)\ p - g_0 E^2 = 0. \tag{41}$$

The roots of the polynomial will give the fixed point solutions for x, y, q. Considering the roots to be $(\bar{x}, \bar{y}, \bar{p}, \bar{q})$, the nature of the fixed points can be understood by considering the time evolution of a small perturbation around these points. We define a small perturbation around the fixed points as $Z_i = k_i - \bar{k}_i$, where $i = 1, 2, 3, 4$ corresponding to $(k_1, k_2, k_3, k_4) \equiv (x, y, p, q)$.

To obtain the time evolution of Z_i, we solve $\dot{Z}_i = \dot{k}_i = f_i(x, y, p, q)$ by expanding the f_i polynomials around the fixed point and retaining the first-order terms as shown below:

$$f_j(x,y,p,q) \approx f_j\Big|_{x,y,p,q=\bar{x},\bar{y},\bar{p},\bar{q}} + \sum_{k=x,y,p,q} (k_i - \bar{k}_i)\frac{\partial f_j}{\partial k_i}\Big|_{x,y,p,q=\bar{x},\bar{y},\bar{p},\bar{q}}. \tag{42}$$

This allows us to obtain the four coupled equations of motion for the small perturbations around fixed points as,

$$\frac{d}{dt}\begin{bmatrix} Z_1 \\ Z_2 \\ Z_3 \\ Z_4 \end{bmatrix} = \begin{bmatrix} \frac{\partial f_1}{\partial x} & \frac{\partial f_1}{\partial y} & \frac{\partial f_1}{\partial p} & \frac{\partial f_1}{\partial q} \\ \frac{\partial f_2}{\partial x} & \frac{\partial f_2}{\partial y} & \frac{\partial f_2}{\partial p} & \frac{\partial f_2}{\partial q} \\ \frac{\partial f_3}{\partial x} & \frac{\partial f_3}{\partial y} & \frac{\partial f_3}{\partial p} & \frac{\partial f_3}{\partial q} \\ \frac{\partial f_4}{\partial x} & \frac{\partial f_4}{\partial y} & \frac{\partial f_4}{\partial p} & \frac{\partial f_4}{\partial q} \end{bmatrix} \begin{bmatrix} Z_1 \\ Z_2 \\ Z_3 \\ Z_4 \end{bmatrix}. \tag{43}$$

Upon substituting the values of f_i's, and evaluating the derivative at the fixed points, we get

$$\frac{d}{dt}\begin{bmatrix} Z_1 \\ Z_2 \\ Z_3 \\ Z_4 \end{bmatrix} = S \begin{bmatrix} Z_1 \\ Z_2 \\ Z_3 \\ Z_4 \end{bmatrix}, \tag{44}$$

where the evolution matrix S is given by

$$S = \begin{bmatrix} -\frac{\kappa}{2} - 2\alpha_c\bar{x}\bar{y} & -\Delta - 2g_0\bar{p} - \alpha_c\bar{x}^2 - 3\alpha_c\bar{y}^2 & -2g_0\bar{y} & 0 \\ \Delta + 2g_0\bar{p} + 3\alpha_c\bar{x}^2 + \alpha_c\bar{y}^2 & -\frac{\kappa}{2} + 2\alpha_c\bar{x}\bar{y} & 2g_0\bar{x} & 0 \\ 0 & 0 & -\frac{\gamma_m}{2} & \omega_m \\ 2g_0\bar{x} & 2g_0\bar{y} & -\omega_m & -\frac{\gamma_m}{2} \end{bmatrix} \tag{45}$$

The solution of the matrix equation will have the following form,

$$Z(t) = \sum_{i=1}^{4} c_i W_i \exp \lambda_i t, \tag{46}$$

where c_i's are the constants of integration, W_i's and λ_i' are the eigenvectors and eigenvalues of the matrix S.

From Eq. 46, it is evident that stable solutions are only possible iff all the eigenvalues have a negative real part. To cross-check the results from the nonlinear optomechanically coupling can be obtained in a straightforward manner by setting α_c to zero, as given by,

$$\frac{d}{dt}\begin{bmatrix} Z_1 \\ Z_2 \\ Z_3 \\ Z_4 \end{bmatrix} = \begin{bmatrix} -\frac{\kappa}{2} & -\Delta - 2g_0\bar{p} & -2g_0\bar{y} & 0 \\ \Delta + 2g_0\bar{p} & -\frac{\kappa}{2} & 2g_0\bar{x} & 0 \\ 0 & 0 & -\frac{\gamma_m}{2} & \omega_m \\ 2g_0\bar{x} & 2g_0\bar{y} & -\omega_m & -\frac{\gamma_m}{2} \end{bmatrix} \begin{bmatrix} Z_1 \\ Z_2 \\ Z_3 \\ Z_4 \end{bmatrix}. \tag{47}$$

Results of these calculations in different limits are shown in Fig. 16(b). We also include a dimensionless power $P = 8g_0^2 n_0/\omega_m^4$ on the right $y-$axis, where n_0 is defined as the number of photons when the pump is set at the cavity frequency [96, 107]. Clearly, the threshold power estimated from the calculations is larger than the one measured in the experiment. For comparison, the instability boundary obtained while considering the optomechanical Kerr nonlinearity alone ($\alpha_c = 0$), and two non-zero values of $\alpha_c/2\pi = 5, 12.5$ mHz/photon are also included. We note that even a significantly higher value of α_c does not fully explain the experimental findings suggesting a different origin. Thus, the nonlinearities arising from the optomechanical interaction and the kinetic inductance do not completely capture the threshold for the unstable region when a linear stability test is applied.

In addition, the numerical calculations do not show the period-doubling bifurcations or chaotic behaviour for the pump parameters used in the experiment. In numerical calculations, these effects appear at higher powers than the ones observed in the experiment. It thus provides the first experimental evidence that the route to chaos in the USC limit or equivalently in the weakly dissipative limit is different from the previously studied cases. It suggests that the role of thermal fluctuations, and residual weak nonlinear coupling terms might be relevant in determining the boundary of the unstable region [111, 112]. In particular, during the transitions from self-oscillation to period-doubling oscillation and subsequently to chaotic regions, the mechanical mode remains in a high amplitude state. In this case, the role of mechanical Duffing nonlinearity, and resonantly-induced negative dissipative might become important [113].

3.11 Summary

We have demonstrated the ultrastrong coupling using a superconducting waveguide cavity and a mechanical resonator, where splitting of the mechanical polaritons becomes nearly 81% of the mechanical frequency. In time-domain, we measure optomechanical swap time of 160 ns, which is nearly 16 times shorter than the smallest dissipation time in the device. With suitable modification to the thermalization of the microwave signals, the cavity can be operated in the quantum limit. It would enable a wide variety of experiments such as the entangled ground state properties of the cavity and the mechanical resonator [92], and high speed optomechanical gates [108]. Using the pump in a pulse mode, the parametric coupling can be pushed beyond the USC regime [91, 114]. In addition, the microwave frequency comb generated using the optomechanical-nonlinearity can be a valuable resource for sensing applications [106]. The experiment here, for the first time, explores the unstable response in the steady-state in the weakly dissipative limit [107]. Clearly, the theoretical model based on optomechanical and kinetic inductance nonlinearity does not account for the lower threshold powers observed in the experiment. It thus opens up the possibility to further explore the role of quantum fluctuations [96], and other weak residual couplings in the interaction Hamiltonian [111].

4 Progress report: January 2023 - August 2023

4.1 Executive summary

Cavity electromechanical systems are extensively used for sensing and controlling the vibrations of a mechanical mode down to their quantum limit. We demonstrate a flux-coupled electromechanical device, where a qubit-cavity dressed mode is used to achieve a magnetic-field-dependent electromechanical coupling. It is established by performing an electromechanically-induced transparency experiment with a dressed-mode occupation of 6×10^{-3} photon. We reach the single-photon coupling rate of 60 kHz, which is nearly 1.5% of the mechanical mode frequency. With increase in the pump strength, the dressed-mode shows the signature of "super-splitting", and strong backaction on the mechanical resonator. It is reflected in the broadening of the mechanical linewidth by a factor of 42 while using fewer than 1 photon in the dressed mode. The manifestation of strong backaction on the mechanical resonator in the sub-photon regime takes us one step closer to the nonlinear quantum optomechanics regime.

4.2 Introduction

Light carries momentum, and it can be used to control and manipulate the motion of a mechanical resonator down the quantum regime [44]. Such control over the motional states is essential for the technological advancement as well as to probe the fundamental physics [115, 116]. One of the leading platforms for light-matter interaction is electromechanical devices, where an electromagnetic(EM) mode is coupled to a mechanical resonator [44, 6]. In the microwave domain, the vibrations of the mechanical resonators are integrated into the EM mode using different strategies like the piezoelectric effect, and the charge modulation. Such devices have been quite successful in demonstrating the sideband cooling of the mechanical resonator to the ground state [45], precise measurement beyond standard quantum limit [117], preparation of non classical states [47, 108, 118, 119], entanglement between two mechanical oscillators [49, 50], and the parametric ultra-strong coupling [32, 120].

Another fundamentally different way to couple the mechanical resonators to an EM mode is to use magnetic flux modulation via Josephson inductance [121]. Apart from providing the electromechanical coupling, the nonlinear nature of the Josephson inductance can be a valuable resource. Indeed, recent experiments have shown large electromechanical coupling rates [65, 68, 66] and the near ground state cooling of the mechanical resonator by four-wave-mixing [69], and by Kerr-enhanced techniques [122]. Further, such flux-coupled electromechanical devices have been proposed to reach the single-photon strong coupling regime using its linear scaling with the magnetic field [123, 55, 74]. Thus far, most of these experiments have largely focused on the weak participation of the Josephson inductance to the total inductance of the EM mode. In such a limit, the dynamics can largely be understood by treating the EM mode as a weak-Kerr oscillator, or by considering the Kerr quasi-modes [69, 122].

Here, we demonstrate an electromechanical device using a linear cavity, a frequency tunable transmon qubit, and a mechanical resonator. The transmon qubit is realized by dc-SQUID, shunted by a suitable capacitance, and the mechanical resonator is implemented as a suspending arm of the SQUID loop [68]. Tuning of the transmon qubit in resonance with the cavity results into the formation of the new eigenstates due to the designed strong coupling. Both the new eigenstates show the flux-tuning, and share the nonlinearity of the Josephson inductance, referred as Jaynes-Cummings nonlinearity [124, 125]. In the low dissipation limit and at higher powers, the dressed mode can get further dressed with the drive photons and can exhibit multiple-peaks, sometimes referred to as “super-splitting”, which at sufficiently large drive powers converge to the bare linear cavity mode [126, 127]. Thus, at high powers, the dynamics of the dressed mode is remarkably different than of a weak-Kerr oscillator, which shows the frequency softening and bifurcation.

The experiment discussed here uses the flux-tunability and the non-trivial high power response of the dressed mode and investigate its backaction on the mechanical resonator. We observe interference feature in EIT-like measurement scheme while having mean occupation of the dressed mode as low as 0.01 photons and estimate single photon electromechanical rate up to 60 kHz. At high pump powers, we observe the signature of super-splitting of the dressed mode, and a strong back-action on the mechanical mode. Further, we conclusively show that a model based on the Kerr-nonlinearity is not sufficient to explain the experimental observations.

4.3 Device concept

Our device consists of a frequency tunable transmon qubit, enabled by a SQUID loop, and it couples to a coaxial cavity. Fig. 17a shows the schematic design of the device. The coaxial cavity is placed inside a 2-axis vector magnet, allowing us to control the axial and the normal components of the magnetic field independently. The cavity is machined from oxygen-free high thermal conductivity copper, and has a bare resonance frequency of 5.846 GHz. The qubit is fabricated on an intrinsic silicon chip using electron beam lithography(EBL), followed by a shadow evaporation of aluminium and *in situ* oxidation. To achieve a larger critical in-plane magnetic field, we use 28 nm thin Al film to fabricate the device[77]. The mechanical resonator is realized by suspending one of the arms of the SQUID loop by selective isotropic dry etching of the silicon substrate. The transmon is designed to have a maximum frequency of 7.4 GHz, which can be tuned by varying the external magnetic flux through the SQUID loop.

A false color scanning electron microscope image of the SQUID loop with the suspended mechanical resonator is shown in Fig. 17b. The patterned chip is placed inside the coaxial cavity and cooled down to 20 mK in a dilution refrigerator. Since superconducting films show more resilience to the in-plane magnetic field [77], we focus on the electromechanical coupling of the out-of-plane vibrational mode of the mechanical resonator. Further, by using the control over the normal component of the magnetic field, we can cancel any out-of-plane component of the magnetic field arising from the misalignment between the axial field and SQUID plane.

When the qubit is made resonant with the cavity, new eigenstates emerge, which are the symmetric and anti-symmetric combination of single excitation states of the qubit and cavity, denoted by $|+\rangle$ and $|-\rangle$ in Fig. 17c. As mentioned earlier, these eigenstates

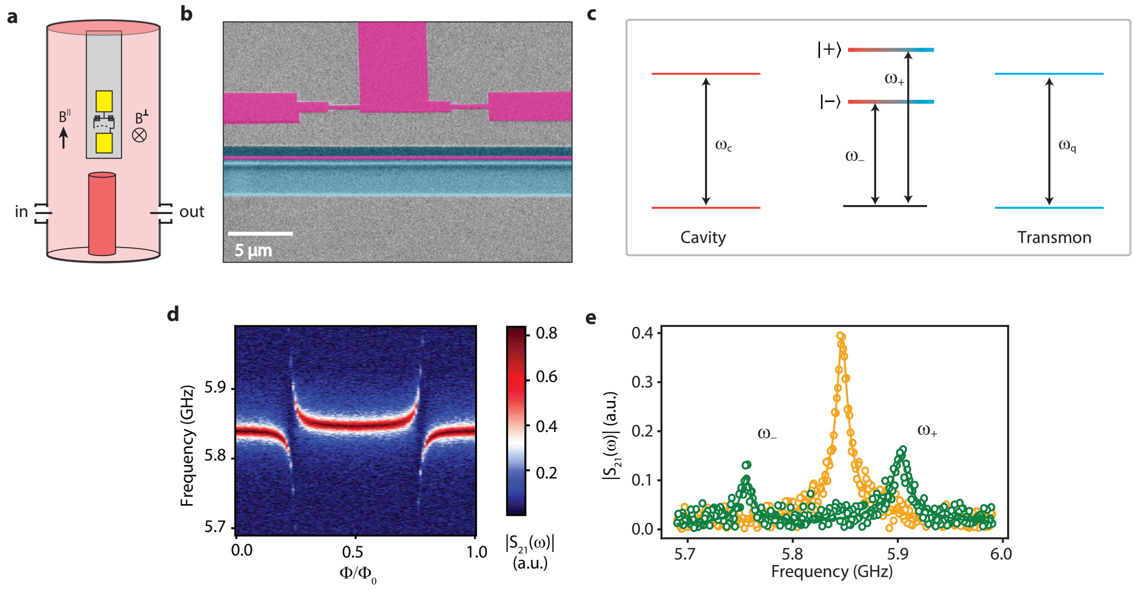

Figure 17: **Device concept:** (a) A schematic view of a quarter wavelength coaxial cavity (in red) coupled to a transmon qubit (in yellow). The two pads provide the shunting capacitance to the transmon as well as providing coupling to the fundamental mode of the cavity. The axial and normal components of the magnetic-field are denoted by $B^{\parallel}$ and $B^{\perp}$, respectively. (b) A false-color scanning electron microscope image of the SQUID loop with embedded mechanical resonator. The two Josephson junctions and part of the suspended beam can be seen. Thin Al film and the silicon substrate are shown in pink and gray colors, respectively. The selectively etched region of silicon is shown by the cyan-colored region. The mechanical resonator has dimensions of 40 μm$\times$200 nm$\times$28 nm. (c) The energy-level diagram depicts the vacuum Rabi splitting. The cavity and transmon frequencies are denoted by ω_c and ω_q, respectively. In the resonant limit $\omega_q \simeq \omega_c$, the transition frequencies of the vacuum Rabi split modes are indicated by ω_+ and ω_-. (d) Colorplot of the cavity voltage transmission $|S_{21}|$ when flux through the SQUID loop is varied. (e) The panel shows two linecuts from panel-d, corresponding to $\Phi/\Phi_0 = 0.5$ and $\Phi/\Phi_0 = 0.27$ in yellow and green color, respectively. The solid-lines are the fitted curves. At $\Phi/\Phi_0 = 0.5$, the qubit significantly detuned from the cavity, and a nearly "cavity-like" mode is observed. For $\Phi/\Phi_0 = 0.27$, the qubit and cavity become nearly resonant, and transmission measurement shows the vacuum Rabi split peaks.

retain the flux-tunability of the qubit and the Josephson nonlinearity is distributed in both the modes. Thus, each dressed mode can be treated as an effective two-level system and can be used for the electromechanical coupling. Considering the higher frequency dressed mode alone, the effective Hamiltonian can be written as,

$$H \simeq \omega_+\Sigma_z + \omega_m b^\dagger b + g_+\Sigma_z(b + b^\dagger), \tag{48}$$

where ω_+, ω_m, and g_+ are dressed mode frequency, mechanical mode frequency, and single-photon electromechanical coupling rate, respectively. The ladder operators for the mechanical mode, and the Pauli operator for the dressed mode are denoted by $b(b^\dagger)$, and Σ_z, respectively.

4.4 Measurements

We begin by measuring the voltage transmission $|S_{21}(\omega)|$ through the cavity while varying the magnetic flux through the SQUID loop. Depending on the flux passing through the SQUID loop, the qubit frequency can vary from its maximum value to a minimum value. Fig. 17d shows the color plot of the cavity transmission. As the qubit is brought in resonance with the cavity, the measured transmission splits into two well-separated dressed modes as shown in Fig. 17e, demonstrating the strong coupling. Provided low strength of the input power, the dressed cavity mode for $\Phi/\Phi_0 = 0.5$, and the vacuum Rabi-split peaks(VRS) for $\Phi/\Phi_0 = 0.27$ have the characteristic Lorentzian lineshape. From the separation of VRS, we infer the strength of the qubit-cavity coupling to be 72 MHz. The reduction in the peak height of VRS in resonant condition suggests that energy dissipation via the qubit dominates over the cavity dissipation rate (κ), *i.e.* $(\Gamma_1/2 + \Gamma_\phi) \gg \kappa$, where Γ_1 and Γ_ϕ are the energy relaxation and the pure dephasing rates of the qubit, respectively.

For the out-of-plane vibration mode of the mechanical resonator, the single-photon electromechanical coupling rate g_+ can be written as $g_+ = \alpha G_+ B^{\parallel} l x_{zp}$, where $G_+ = d\omega_+/d\Phi$ is the flux responsivity of the upper dressed mode, $B^{\parallel}$ is the axial component of the applied magnetic field, x_{zp} is the quantum zero-point fluctuations of the mechanical resonator and α is a geometrical factor of order unity and depends on the mechanical modeshape. It is evident that higher single-photon electromechanical coupling rate can be achieved by increasing the flux-responsivity and magnetic field $B^{\parallel}$. As evident from Fig. 17d, the increased flux-responsivity of the dressed mode comes at a cost of reduced transmission. Therefore, we choose an optimal operating point on the upper dressed mode $\omega_+/2\pi = 5.884$ GHz, which corresponds to the flux responsivity $G_+/2\pi \approx 1.85$ GHz/Φ_0, and proceed to determine the electromechanical coupling.

4.5 Flux-mediated electromechanical coupling

To probe the electromechanical coupling between the dressed mode and the mechanical resonator, we use the technique utilized for electromagnetic induced transparency (EIT) experiment in the atomic physics [128]. Its mechanical analog in a cavity optomechanical devices, known as optomechanically induced transparency (OMIT) [109]. Fig. 18a shows the schematic of the different transitions involved in the measurement. In this technique,

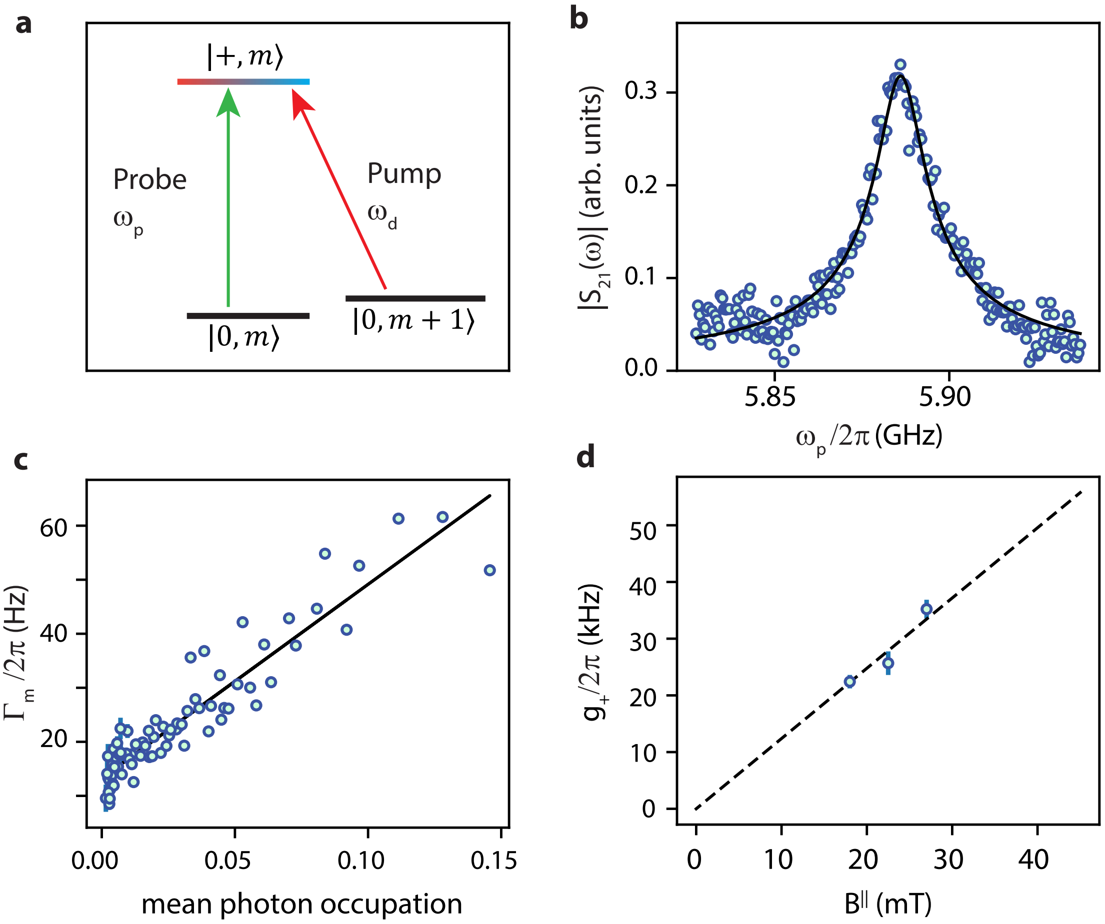

Figure 18: **Electromechanically induced absorption (EIA):** (a) Pump and probe scheme for the EIA experiment. Energy levels of the system and the corresponding drives are shown. The state $|+, m\rangle$ denotes one excitation is in the dressed mode, and m excitation in the mechanical resonator. The pump and probe signals are shown by the red and green arrows, respectively. The pump frequency ω_d is kept fixed and the probe frequency ω_p is swept to measure $|S_{21}(\omega)|$ of the dressed mode. (b) $|S_{21}(\omega)|$ measured in the absence of the pump signal, showing the linear response of the dressed mode. The solid-black line is a Lorentzian fit to the response. (c) Variation of Γ_m is plotted with mean photon occupation of the dressed mode n_d, along with a straight line fit (shown in solid-black line) yielding the single-photon electromechanical coupling rate $g_+ \sim 35$ kHz. The experiment is done with a dressed mode frequency $\omega_+/2\pi \sim 5.884$ GHz and axial magnetic field $B^{\parallel} \sim 27$ mT. (d) Experimentally determined electromechanical coupling rate for three different values of the applied magnetic field $B^{\parallel}$. While increasing $B^{\parallel}$, the flux-responsivity is nominally kept constant by adjusting $B^{\perp}$.

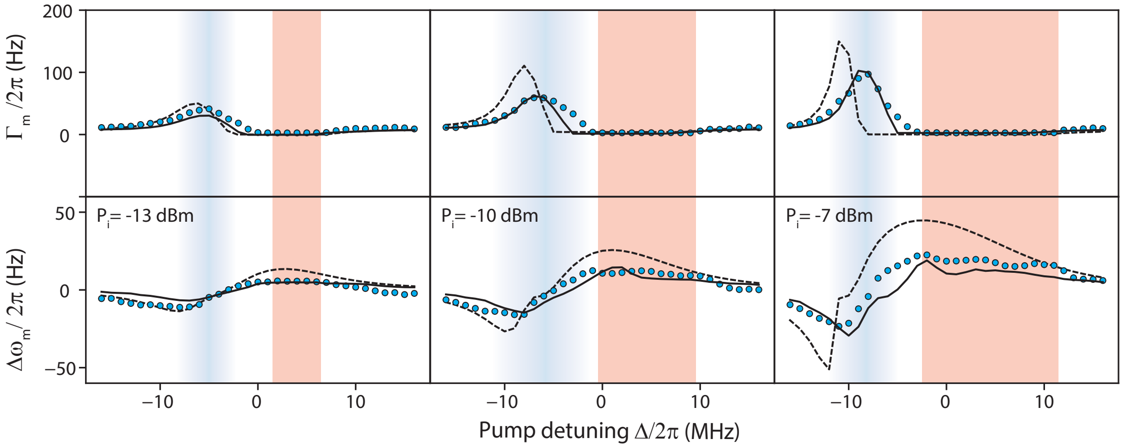

Figure 19: **Dynamical backaction on the mechanical resonator:** Optomechanical damping and spring-shift is plotted with pump detuning. From left to right panel the pump power is increased, which results into stronger backaction. For these measurements, the dressed mode is tuned to $\omega_+/2\pi \sim 5.8734$ GHz and the axial magnetic field is set to $B^{\parallel} \sim 18$ mT. These parameters correspond to a coupling strength of $g_+/2\pi \sim 17$ kHz. The solid circles are the experimental data points. The dashed lines are the results from the theoretical calculations based on a Kerr-like oscillator. The solid-black lines are the results from similar calculations except the circulating power in the dressed mode is obtained from the experiment. The details of both the calculations are given in Supporting Information. The shaded regions denote the cooling and unstable response of the mechanical resonator.

two coherent signals are sent to the device, *i.e.* a pump signal at $(\omega_+ - \omega_m)$ which drives the $|0, m+1\rangle \leftrightarrow |+, m\rangle$ transition, and a weak probe signal at ω_p (near ω_+) to measure the transmission.

Without the pump, the voltage transmission $|S_{21}(\omega_p)|$ has a linear response with characteristic Lorentzian lineshape as shown in Fig. 18b. In the presence of the pump, an absorption feature appear in the transmission spectrum. It arises from the destructive interference of the probe field from two different pathways [129, 109]. We emphasize that due to a high anharmonicity of the dressed mode and low pump strengths used in the experiment, the interference feature effectively arises dominantly from the participation of ground and first excited states of the upper dressed mode, denoted by $|0\rangle$ and $|+\rangle$, respectively. The shape of the absorption feature is determined by the response of the mechanical resonator and can be used to extract its resonant frequency and effective dissipation rate. We estimate the mechanical resonant frequency to be $\omega_m/2\pi \approx 3.97$ MHz.

The mechanical resonator further experiences back-action in the presence of pump signal, and it manifests in the enhanced linewidth of the interference feature. Fig. 18c shows the change in the linewidth of interference feature for different strengths of the pump signal. The effective linewidth of the absorption signal is given by $\Gamma_m = \gamma_m(1 + C)$ [53], where γ_m is intrinsic mechanical linewidth, $C = 4g_+^2 n_d/(\kappa\gamma_m)$ is the optomechanical cooperativity and κ is the energy decay rate of the dressed mode. The quantity n_d represents the mean circulating power in the dressed mode in the units of $\hbar\omega_d$ equivalently, the mean photon occupation of the dressed mode. It can be calibrated to a good accuracy by tuning the qubit in the dispersive regime, and performing *ac*-Stark shift measurements.

As shown in Fig. 18c, the plot of the effective mechanical linewidth Γ_m with n_d yields the slope $4g_+^2/\kappa$, and thus g_+ . From the slop, we estimated the single-photon electromechanical coupling rate $g_+/2\pi \sim$ 35 kHz, obtained at the axial field of $B^{\parallel} \sim$ 27 mT. The intercept of the straight line fit in Fig. 18c gives the intrinsic mechanical linewidth $\gamma_m/2\pi \sim 13$ Hz. Further, at the lower magnetic fields and lower flux responsive operating points, we measure an intrinsic mechanical linewidth as low as $\gamma_m/2\pi \sim 6$ Hz.

Since the single-photon electromechanical coupling rate is linearly proportional to the axial magnetic field $B^{\parallel}$, we carry out similar interference experiments at different magnetic fields, and estimate the single photon electromechanical coupling rates. Fig. 18d shows the plot of experimentally determined g_+ for different values of the magnetic field. A straight-line extrapolation of the data suggest our system achieves a very high coupling rate $g_+/2\pi \sim 60$ kHz for a magnetic field $B^{\parallel} \sim 45$ mT, which was the maximum applied magnetic field in our experiment. As discussed in the next section, such a high coupling can be a valuable resource in the active sideband cooling of the mechanical resonator using just a few photons in the dressed mode.

4.6 Strong backaction and sideband cooling: Beyond the linear response

To further investigate the effect of dynamical backaction on the mechanical resonator, we send a pump signal, and measure the power spectral density(PSD) of the output microwave signal while varying the pump detuning for different pump powers. Depending on the pump detuning, an imbalance between the up- and down-scattering rates of microwave photons by the mechanical resonator is achieved, which leads to its cooling or heating. Initially, we operate at a lower magnetic field of $B^{\parallel} \sim 18$ mT, and at a reduced flux responsivity of $G_+/2\pi \sim 1.1$ GHz/Φ_0, which corresponds to $g_+/2\pi \sim 15$ kHz. Fig. 19 shows the measurements of the effective mechanical linewidth and the shift in the mechanical frequency as the pump detuning and amplitude are varied. As expected, we observe a broadening of the mechanical linewidth for negative detunings and an unstable response for the positive detunings. Further, as the strength of the pump signal is increased, the backaction effects becomes enhanced, and the onset of unstable response shifts towards negative detuning due to the Josephson nonlinearity.

To theoretically understand the experimental observations, we model the dressed mode as a weakly nonlinear oscillator by including a Kerr-term. Effectively, the total Hamiltonian of the system can be written as $H = -\Delta\hat{a}^\dagger\hat{a} - \alpha_c\hat{a}^\dagger\hat{a}^\dagger\hat{a}\hat{a}/2 + \omega_m\hat{b}^\dagger\hat{b} + g_+ \; \hat{a}^\dagger\hat{a}(\hat{b}+\hat{b}^\dagger) + \epsilon\;(\hat{a}+\hat{a}^\dagger)$, where α_c is the Kerr-nonlinearity, ϵ is the pump amplitude, Δ is the pump detuning from ω_+, and $\hat{a}(\hat{a}^\dagger)$ is the lowering (raising) operator of the upper dressed mode. For simplicity, we neglect the lower dressed mode due to its large detuning. To compute the backaction effects on the mechanical resonator, we solve the equations of motion for the coupled modes and obtain the expressions of the effective linewidth and the frequency shift of the mechanical resonator. The dashed lines in Fig. 19 show the theoretically calculated results using a Kerr nonlinearity of $\alpha_c/2\pi \sim$ 5.1 MHz/photon. In addition, for the calculations of effective linewidth and frequency shift, we can also use the experimentally determined value of the circulating power, estimated from mode transmission $|S_{21}(\omega)|$. Since the input line attenuation, the input/output port couplings, and net output gain of the cavity can be calibrated, it becomes straightforward to compute the circulating power $n_d\hbar\omega_d$ in the dressed mode. Solid black lines in Fig. 19 are theoretical results based on experimentally determined $n_d\hbar\omega_d$. It is evident from Fig. 19 that a weak Kerr oscillator model does not predict the backaction effects accurately at higher pump powers while the calculation taking into account the actual mode transmission matches better with the experimental results.

As mentioned earlier, a Kerr-nonlinear oscillator shows a Duffing response before showing bifurcations, however, the power response of the vacuum dressed split modes is very different. In the dispersive limit $|\omega_q - \omega_c| \gg g$, the high power response has been explained by considering the unconfined states of the transmon qubit [25, 130]. In the weakly dissipative resonant limit, it is explained by the "dressing" of the dressed mode with the drive photons, usually referred to as "super-splitting". It results in a series of additional peaks arising from the multi-photon transitions [124]. At sufficiently high powers, the multi-photon transitions are spaced closely to the bare cavity transition due to enhanced loss or temperature, and thus results in a classical bare cavity response [127].

We observe a non-trivial response of the dressed mode, when we tune the dressed mode to 5.884 GHz, and $B^{\parallel}$ to 45 mT to explore strong back action on the mechanical resonator. This is due to the fact that the dressed mode has a higher Kerr-nonlinearity $\alpha_c/\pi \sim$ 13.2 MHz/photon at this detuning. As shown in Fig. 20a, the linear response (top panel) of the dressed mode becomes quite complex and shows multiple peaks (middle panel) when the pump is increased to -4 dBm. These peaks arise from the super-splitting of the dressed mode , and are not well-resolved due to larger qubit dissipation and dephasing rates. At higher power, the response again becomes Lorentzian showing the

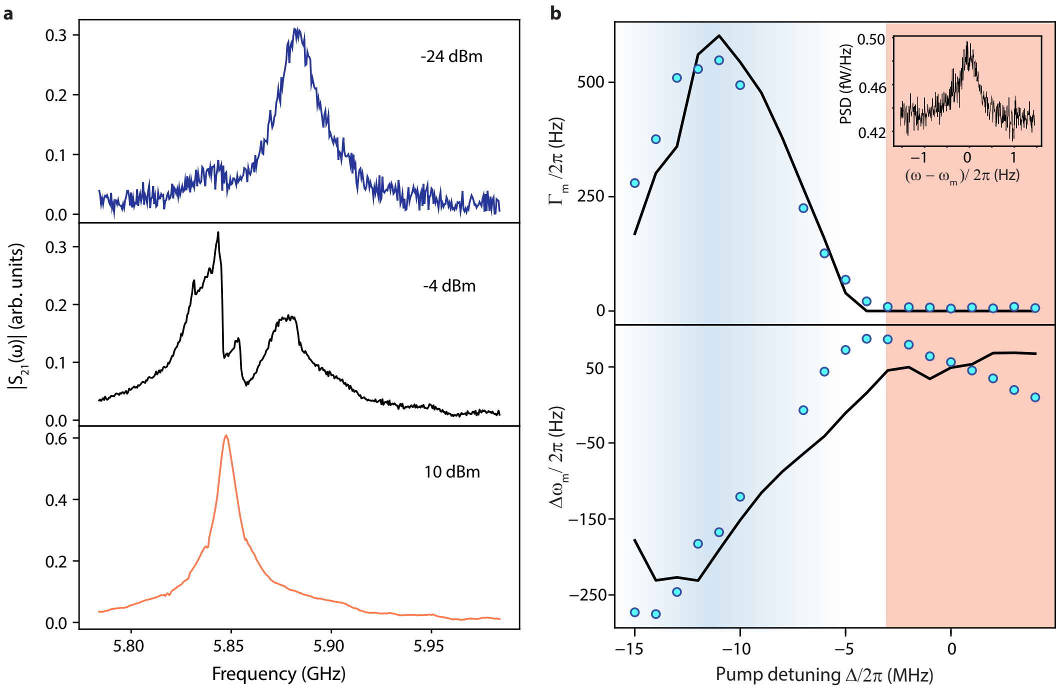

Figure 20: **Strong Backaction:** (a) The response of the dressed mode at large axial magnetic field $B^{\|} \sim 45$ mT. The top panel shows the linear response at low input power of -24 dBm which is a Lorentzian at the resonant frequency of $\omega_+/2\pi \sim 5.884$ GHz. The middle panel shows the dressed mode response at relatively higher power of -4 dBm where multiple overlapping peaks arising from the super-splitting of dressed mode can be seen. With further increase in the power to +10 dBm, the bare cavity response with Lorentzian lineshape is recovered as shown in the bottom panel. (b) Shows the backaction results on the mechanical resonator for the pump power corresponding to the middle panel of (a). The solid black curves are the results from theoretical calculations based on the experimentally determined circulating power in the dressed mode. The shaded regions denote the cooling and the unstable response of the mechanical resonator. The inset shows the thermal spectrum of the mechanical resonator corresponding to the maximum cooling at a pump detuning of $\Delta \approx -3.5\omega_m$.

bare-cavity mode (lowest panel)

At this operating point, the estimated single-photon coupling rate $g_+/2\pi$ becomes 60 kHz. Consequently, it results in enhanced backaction on the mechanical resonator as shown in Fig. 20b. In addition, the dressed mode's high nonlinearity causes the boundary of the unstable response to shift further towards the negative pump detunings. To understand the experimental results, we again use the transmission measurements $|S_{21}(\omega)|$ performed at a fixed input power, and compute the circulating power in the microwave mode. The solid black curves in Fig. 20b show the calculated results. We see that the theoretical calculations show minor deviation from the experimental results. To fully understand this aspect, a treatment of the backaction considering the Jaynes-Cummings nonlinearity might be required.

The inset of Fig. 20b, we show the mechanical resonator's spectrum when the backaction is strongest. We observe that the mechanical linewidth broadens to 550 Hz at $\Delta \approx -3.5\omega_m$, which is an enhancement of 42 times over the intrinsic mechanical linewidth. The circulating power in the microwave mode is remarkably low, and it is equivalent to the mean occupation of 0.7 photons. We emphasize here that due to large electromechanical coupling, we observe such a strong backaction with less than one photon in the dressed mode.

We next try to estimate the effective mechanical phonon occupation corresponding to the effective linewidth of 550 Hz. We first establish the effective mechanical temperature by measuring the thermal power spectral density using a weak pump signal at zero detuning such that backaction effects can be neglected. We estimate that the mechanical mode is thermalized to 70 mK, corresponding to an average phonon occupation of ~ 365 (details in S3). We then extend our analysis based on the estimation of the circulating power from the transmission measurement. Assuming no multi-photon loss or microwave gain, we convert the thermo-mechanical power spectral density to the mean phonon occupation. We estimated the mean phonon occupancy of 8.6 for the maximum cooling of the mechanical resonator.

4.7 Discussion

To summarize, the performance of the flux-coupled electromechanical device has been enhanced using the strong nonlinearity of the superconducting transmon qubit. This has been largely made possible by fabricating the device with thin film of aluminium (28 nm), which provides strong resilience against the magnetic field and also results in lower mass of the mechanical resonator ($\sim$ 0.75 pg). The combined effects result in large single-photon coupling rate $g_+/2\pi \sim 60$ kHz, which is an order of magnitude improvement over the previously demonstrated flux coupled devices[65, 68, 66, 122]. Due to such a large single-photon electromechanical coupling rate, we could observe the electromechanically-induced interference feature at extremely low ($< 10^{-2}$) photon occupations, which is lower by several orders of magnitude as compared to all the previous implementations of electromechanical devices. We further observe the signature of the super-splitting of the dressed modes, and utilize their nonlinearity to observe a strong backaction on the mechanical oscillator.

Looking ahead, given that transmon qubits have been shown to operate in the magnetic fields as high as 1 T [77], one can envision devices that can operate in a regime where the single-photon coupling rate becomes comparable to the mechanical resonant frequency. While the sideband cooling performance in the current experiment is limited due to the lower sideband-resolution parameter $\omega_m/\kappa \approx 0.25$. It can easily be improved by making smaller length mechanical resonator, resulting in higher mechanical resonant frequency. With such promising futuristic parameters, it is feasible to achieve ground state cooling via sideband driving below the level of a single photon, and it further suggests ways to prepare non-classical mechanical states including Schrodinger-cat [55, 74]. Even with the existing parameters, solely by improving qubit and cavity coherence, it is possible to prepare mechanical Fock and cat states[131]. Such methods thus open up ways to use the mechanical resonators for quantum information storage utilizing their long coherence times. Finally, such techniques can be extended to the low frequency flux-family superconducting qubits to realize transverse electromechanical couplings, and thus extending the toolbox available with the flux-coupled devices [132].

References

[1] M. A. Castellanos-Beltran and K. W. Lehnert. Widely tunable parametric amplifier based on a superconducting quantum interference device array resonator. *Applied Physics Letters*, 91(8):083509, 2007.

[2] T. Yamamoto, K. Inomata, M. Watanabe, K. Matsuba, T. Miyazaki, W. D. Oliver, Y. Nakamura, and J. S. Tsai. Flux-driven Josephson parametric amplifier. *Applied Physics Letters*, 93(4):042510, 2008.

[3] C. Macklin, K. O'Brien, D. Hover, M. E. Schwartz, V. Bolkhovsky, X. Zhang, W. D. Oliver, and I. Siddiqi. A near–quantum-limited Josephson traveling-wave parametric amplifier. *Science*, 350(6258):307–310, 2015.

[4] Michel H. Devoret and John M. Martinis. Implementing Qubits with Superconducting Integrated Circuits. *Quantum Information Processing*, 3(1-5):163–203, 2004.

[5] Alexandre Blais, Jay Gambetta, A. Wallraff, D. I. Schuster, S. M. Girvin, M. H. Devoret, and R. J. Schoelkopf. Quantum-information processing with circuit quantum electrodynamics. *Physical Review A*, 75(3):032329, 2007.

[6] A. A. Clerk, K. W. Lehnert, P. Bertet, J. R. Petta, and Y. Nakamura. Hybrid quantum systems with circuit quantum electrodynamics. *Nature Physics*, 16(3):257–267, 2020.

[7] Iulia Buluta, Sahel Ashhab, and Franco Nori. Natural and artificial atoms for quantum computation. *Reports on Progress in Physics*, 74(10):104401, 2011.

[8] Ze-Liang Xiang, Sahel Ashhab, J. Q. You, and Franco Nori. Hybrid quantum circuits: Superconducting circuits interacting with other quantum systems. *Reviews of Modern Physics*, 85(2):623–653, 2013.

[9] Emmanuel Flurin, Nicolas Roch, Francois Mallet, Michel H. Devoret, and Benjamin Huard. Generating Entangled Microwave Radiation Over Two Transmission Lines. *Physical Review Letters*, 109(18), 2012.

[10] Baleegh Abdo, Katrina Sliwa, Flavius Schackert, Nicolas Bergeal, Michael Hatridge, Luigi Frunzio, A. Douglas Stone, and Michel Devoret. Full Coherent Frequency Conversion between Two Propagating Microwave Modes. *Physical Review Letters*, 110(17):173902, 2013.

[11] Z. Leghtas, S. Touzard, I. M. Pop, A. Kou, B. Vlastakis, A. Petrenko, K. M. Sliwa, A. Narla, S. Shankar, M. J. Hatridge, M. Reagor, L. Frunzio, R. J. Schoelkopf, M. Mirrahimi, and M. H. Devoret. Confining the state of light to a quantum manifold by engineered two-photon loss. *Science*, 347(6224):853–857, 2015.

[12] M. D. LaHaye, J. Suh, P. M. Echternach, K. C. Schwab, and M. L. Roukes. Nanomechanical measurements of a superconducting qubit. *Nature*, 459(7249):960–964, 2009.

[13] A. D. O'Connell, M. Hofheinz, M. Ansmann, Radoslaw C. Bialczak, M. Lenander, Erik Lucero, M. Neeley, D. Sank, H. Wang, M. Weides, J. Wenner, John M. Martinis, and A. N. Cleland. Quantum ground state and single-phonon control of a mechanical resonator. *Nature*, 464(7289):697–703, 2010.

[14] F. Lecocq, J. D. Teufel, J. Aumentado, and R. W. Simmonds. Resolving the vacuum fluctuations of an optomechanical system using an artificial atom. *Nature Physics*, 11(8):635–639, 2015.

[15] J.-M. Pirkkalainen, S. U. Cho, Jian Li, G. S. Paraoanu, P. J. Hakonen, and M. A. Sillanpää. Hybrid circuit cavity quantum electrodynamics with a micromechanical resonator. *Nature*, 494(7436):211–215, 2013.

[16] Xiaobo Zhu, Shiro Saito, Alexander Kemp, Kosuke Kakuyanagi, Shin-ichi Karimoto, Hayato Nakano, William J. Munro, Yasuhiro Tokura, Mark S. Everitt, Kae Nemoto, Makoto Kasu, Norikazu Mizuochi, and Kouichi Semba. Coherent coupling of a superconducting flux qubit to an electron spin ensemble in diamond. *Nature*, 478(7368), 2011.

[17] Y. Kubo, C. Grezes, A. Dewes, T. Umeda, J. Isoya, H. Sumiya, N. Morishita, H. Abe, S. Onoda, T. Ohshima, V. Jacques, A. Dréau, J.-F. Roch, I. Diniz, A. Auffeves, D. Vion, D. Esteve, and P. Bertet. Hybrid Quantum Circuit with a Superconducting Qubit Coupled to a Spin Ensemble. *Physical Review Letters*, 107(22):220501, 2011.

[18] Martin V. Gustafsson, Thomas Aref, Anton Frisk Kockum, Maria K. Ekström, Göran Johansson, and Per Delsing. Propagating phonons coupled to an artificial atom. *Science*, 346(6206):207–211, 2014.

[19] Riccardo Manenti, Anton F. Kockum, Andrew Patterson, Tanja Behrle, Joseph Rahamim, Giovanna Tancredi, Franco Nori, and Peter J. Leek. Circuit quantum

acoustodynamics with surface acoustic waves. *Nature Communications*, 8(1):975, 2017.

[20] Aleksey N. Bolgar, Julia I. Zotova, Daniil D. Kirichenko, Ilia S. Besedin, Aleksander V. Semenov, Rais S. Shaikhaidarov, and Oleg V. Astafiev. Quantum Regime of a Two-Dimensional Phonon Cavity. *Physical Review Letters*, 120(22):223603, 2018.

[21] Yutaka Tabuchi, Seiichiro Ishino, Atsushi Noguchi, Toyofumi Ishikawa, Rekishu Yamazaki, Koji Usami, and Yasunobu Nakamura. Coherent coupling between a ferromagnetic magnon and a superconducting qubit. *Science*, 349(6246):405–408, 2015.

[22] J. J. Viennot, X. Ma, and K. W. Lehnert. Phonon-Number-Sensitive Electromechanics. *Physical Review Letters*, 121(18):183601, 2018.

[23] Yiwen Chu, Prashanta Kharel, Taekwan Yoon, Luigi Frunzio, Peter T. Rakich, and Robert J. Schoelkopf. Creation and control of multi-phonon Fock states in a bulk acoustic-wave resonator. *Nature*, 563(7733):666, 2018.

[24] Patricio Arrangoiz-Arriola, E. Alex Wollack, Zhaoyou Wang, Marek Pechal, Wentao Jiang, Timothy P. McKenna, Jeremy D. Witmer, Raphaël Van Laer, and Amir H. Safavi-Naeini. Resolving the energy levels of a nanomechanical oscillator. *Nature*, 571(7766):537–540, 2019.

[25] Raphaël Lescanne, Lucas Verney, Quentin Ficheux, Michel H. Devoret, Benjamin Huard, Mazyar Mirrahimi, and Zaki Leghtas. Escape of a Driven Quantum Josephson Circuit into Unconfined States. *Physical Review Applied*, 11(1):014030, 2019.

[26] Lucas Verney, Raphaël Lescanne, Michel H. Devoret, Zaki Leghtas, and Mazyar Mirrahimi. Structural Instability of Driven Josephson Circuits Prevented by an Inductive Shunt. *Physical Review Applied*, 11(2):024003, 2019.

[27] O. Gargiulo, S. Oleschko, J. Prat-Camps, M. Zanner, and G. Kirchmair. Fast flux control of 3D transmon qubits using a magnetic hose. *Applied Physics Letters*, 118(1):012601, 2021.

[28] Yarema Reshitnyk, Markus Jerger, and Arkady Fedorov. 3D microwave cavity with magnetic flux control and enhanced quality factor. *EPJ Quantum Technology*, 3(1):1–6, 2016.

[29] Mingyun Yuan, Vibhor Singh, Yaroslav M. Blanter, and Gary A. Steele. Large cooperativity and microkelvin cooling with a three-dimensional optomechanical cavity. *Nature Communications*, 6:8491, 2015.

[30] Atsushi Noguchi, Rekishu Yamazaki, Manabu Ataka, Hiroyuki Fujita, Yutaka Tabuchi, Toyofumi Ishikawa, Koji Usami, and Yasunobu Nakamura. Ground state cooling of a quantum electromechanical system with a silicon nitride membrane in a 3D loop-gap cavity. *New Journal of Physics*, 18(10):103036, 2016.

[31] Bindu Gunupudi, Soumya Ranjan Das, Rohit Navarathna, Sudhir Kumar Sahu, Sourav Majumder, and Vibhor Singh. Optomechanical Platform with a Three-dimensional Waveguide Cavity. *Physical Review Applied*, 11(2):024067, 2019.

[32] G. A. Peterson, S. Kotler, F. Lecocq, K. Cicak, X. Y. Jin, R. W. Simmonds, J. Aumentado, and J. D. Teufel. Ultrastrong Parametric Coupling between a Superconducting Cavity and a Mechanical Resonator. *Physical Review Letters*, 123(24):247701, 2019.

[33] Nissim Ofek, Andrei Petrenko, Reinier Heeres, Philip Reinhold, Zaki Leghtas, Brian Vlastakis, Yehan Liu, Luigi Frunzio, S. M. Girvin, L. Jiang, Mazyar Mirrahimi, M. H. Devoret, and R. J. Schoelkopf. Extending the lifetime of a quantum bit with error correction in superconducting circuits. *Nature*, 536(7617):441–445, 2016.

[34] Reinier W. Heeres, Philip Reinhold, Nissim Ofek, Luigi Frunzio, Liang Jiang, Michel H. Devoret, and Robert J. Schoelkopf. Implementing a universal gate set on a logical qubit encoded in an oscillator. *Nature Communications*, 8(1):94, 2017.

[35] Hanhee Paik, D. I. Schuster, Lev S. Bishop, G. Kirchmair, G. Catelani, A. P. Sears, B. R. Johnson, M. J. Reagor, L. Frunzio, L. I. Glazman, S. M. Girvin, M. H. Devoret, and R. J. Schoelkopf. Observation of High Coherence in Josephson Junction Qubits Measured in a Three-Dimensional Circuit QED Architecture. *Physical Review Letters*, 107(24):240501, 2011.

[36] K. Juliusson, S. Bernon, X. Zhou, V. Schmitt, H. le Sueur, P. Bertet, D. Vion, M. Mirrahimi, P. Rouchon, and D. Esteve. Manipulating Fock states of a harmonic oscillator while preserving its linearity. *Physical Review A*, 94(6):063861, 2016.

[37] Simon E. Nigg, Hanhee Paik, Brian Vlastakis, Gerhard Kirchmair, S. Shankar, Luigi Frunzio, M. H. Devoret, R. J. Schoelkopf, and S. M. Girvin. Black-Box Superconducting Circuit Quantization. *Physical Review Letters*, 108(24):240502, 2012.

[38] C. Navau, J. Prat-Camps, O. Romero-Isart, J. I. Cirac, and A. Sanchez. Long-Distance Transfer and Routing of Static Magnetic Fields. *Physical Review Letters*, 112(25):253901, 2014.

[39] Peter Groszkowski and Jens Koch. Scqubits: a Python package for superconducting qubits. *Quantum*, 5:583, 2021.

[40] Jens Koch, Terri M. Yu, Jay Gambetta, A. A. Houck, D. I. Schuster, J. Majer, Alexandre Blais, M. H. Devoret, S. M. Girvin, and R. J. Schoelkopf. Charge-insensitive qubit design derived from the Cooper pair box. *Physical Review A*, 76(4):042319, 2007.

[41] R. Bianchetti, S. Filipp, M. Baur, J. M. Fink, M. Göppl, P. J. Leek, L. Steffen, A. Blais, and A. Wallraff. Dynamics of dispersive single-qubit readout in circuit quantum electrodynamics. *Physical Review A*, 80(4):043840, 2009.

[42] J. R. Johansson, P. D. Nation, and Franco Nori. QuTiP: An open-source Python framework for the dynamics of open quantum systems. *Computer Physics Communications*, 183(8):1760–1772, 2012.

[43] Shabir Barzanjeh, André Xuereb, Simon Gröblacher, Mauro Paternostro, Cindy A. Regal, and Eva M. Weig. Optomechanics for quantum technologies. *Nature Physics*, 18(1):15–24, 2022.

[44] Markus Aspelmeyer, Tobias J. Kippenberg, and Florian Marquardt. Cavity optomechanics. *Reviews of Modern Physics*, 86(4):1391–1452, 2014.

[45] J. D. Teufel, T. Donner, Dale Li, J. W. Harlow, M. S. Allman, K. Cicak, A. J. Sirois, J. D. Whittaker, K. W. Lehnert, and R. W. Simmonds. Sideband cooling of micromechanical motion to the quantum ground state. *Nature*, 475(7356):359–363, 2011.

[46] Jasper Chan, T. P. Mayer Alegre, Amir H. Safavi-Naeini, Jeff T. Hill, Alex Krause, Simon Gröblacher, Markus Aspelmeyer, and Oskar Painter. Laser cooling of a nanomechanical oscillator into its quantum ground state. *Nature*, 478(7367):89–92, 2011.

[47] E. E. Wollman, C. U. Lei, A. J. Weinstein, J. Suh, A. Kronwald, F. Marquardt, A. A. Clerk, and K. C. Schwab. Quantum squeezing of motion in a mechanical resonator. *Science*, 349(6251):952–955, 2015.

[48] C. F. Ockeloen-Korppi, E. Damskägg, J.-M. Pirkkalainen, M. Asjad, A. A. Clerk, F. Massel, M. J. Woolley, and M. A. Sillanpää. Stabilized entanglement of massive mechanical oscillators. *Nature*, 556(7702):478–482, 2018.

[49] Shlomi Kotler, Gabriel A. Peterson, Ezad Shojaee, Florent Lecocq, Katarina Cicak, Alex Kwiatkowski, Shawn Geller, Scott Glancy, Emanuel Knill, Raymond W. Simmonds, José Aumentado, and John D. Teufel. Direct observation of deterministic macroscopic entanglement. *Science*, 372(6542):622–625, 2021.

[50] E. Alex Wollack, Agnetta Y. Cleland, Rachel G. Gruenke, Zhaoyou Wang, Patricio Arrangoiz-Arriola, and Amir H. Safavi-Naeini. Quantum state preparation and tomography of entangled mechanical resonators. *Nature*, 604(7906), 2022.

[51] P. Rabl. Photon Blockade Effect in Optomechanical Systems. *Physical Review Letters*, 107(6):063601, 2011.

[52] A. Nunnenkamp, K. Børkje, and S. M. Girvin. Single-Photon Optomechanics. *Physical Review Letters*, 107(6):063602, 2011.

[53] P. Rabl. Cooling of mechanical motion with a two-level system: The high-temperature regime. *Physical Review B*, 82(16):165320, 2010.

[54] Ivar Martin, Alexander Shnirman, Lin Tian, and Peter Zoller. Ground-state cooling of mechanical resonators. *Physical Review B*, 69(12):125339, 2004.

[55] K. E. Khosla, M. R. Vanner, N. Ares, and E. A. Laird. Displacemon Electromechanics: How to Detect Quantum Interference in a Nanomechanical Resonator. 8(2):021052, 2018.

[56] Konstanze Jaehne, Klemens Hammerer, and Margareta Wallquist. Ground-state cooling of a nanomechanical resonator via a Cooper-pair box qubit. *New Journal of Physics*, 10(9):095019, 2008.

[57] Julian Hauss, Arkady Fedorov, Stephan André, Valentina Brosco, Carsten Hutter, Robin Kothari, Sunil Yeshwanth, Alexander Shnirman, and Gerd Schön. Dissipation in circuit quantum electrodynamics: lasing and cooling of a low-frequency oscillator. *New Journal of Physics*, 10(9):095018, 2008.

[58] Ying-Dan Wang, Yong Li, Fei Xue, C. Bruder, and K. Semba. Cooling a micromechanical resonator by quantum back-action from a noisy qubit. *Physical Review B*, 80(14):144508, 2009.

[59] Roson Nongthombam, Ambaresh Sahoo, and Amarendra K. Sarma. Ground-state cooling of a mechanical oscillator via a hybrid electro-optomechanical system. *Physical Review A*, 104(2):023509, 2021.

[60] Xin Wang, Adam Miranowicz, Hong-Rong Li, Fu-Li Li, and Franco Nori. Two-color electromagnetically induced transparency via modulated coupling between a mechanical resonator and a qubit. *Physical Review A*, 98(2):023821, 2018.

[61] Juuso Manninen, Mohammad Tasnimul Haque, David Vitali, and Pertti Hakonen. Enhancement of the optomechanical coupling and Kerr nonlinearity using the Josephson capacitance of a Cooper-pair box. *Physical Review B*, 105(14):144508, 2022.

[62] I. Wilson-Rae, P. Zoller, and A. Imamoḡlu. Laser Cooling of a Nanomechanical Resonator Mode to its Quantum Ground State. *Physical Review Letters*, 92(7):075507, 2004.

[63] P. Rabl, P. Cappellaro, M. V. Gurudev Dutt, L. Jiang, J. R. Maze, and M. D. Lukin. Strong magnetic coupling between an electronic spin qubit and a mechanical resonator. *Physical Review B*, 79(4):041302, 2009.

[64] J.-M. Pirkkalainen, S. U. Cho, F. Massel, J. Tuorila, T. T. Heikkilä, P. J. Hakonen, and M. A. Sillanpää. Cavity optomechanics mediated by a quantum two-level system. *Nature Communications*, 6, 2015.

[65] I. C. Rodrigues, D. Bothner, and G. A. Steele. Coupling microwave photons to a mechanical resonator using quantum interference. *Nature Communications*, 10(1), 2019.

[66] Philip Schmidt, Mohammad T. Amawi, Stefan Pogorzalek, Frank Deppe, Achim Marx, Rudolf Gross, and Hans Huebl. Sideband-resolved resonator electromechanics based on a nonlinear Josephson inductance probed on the single-photon level. *Communications Physics*, 3(1):1–7, 2020.

[67] D. Zoepfl, M. L. Juan, C. M. F. Schneider, and G. Kirchmair. Single-Photon Cooling in Microwave Magnetomechanics. *Physical Review Letters*, 125(2):023601, 2020.

[68] Tanmoy Bera, Sourav Majumder, Sudhir Kumar Sahu, and Vibhor Singh. Large flux-mediated coupling in hybrid electromechanical system with a transmon qubit. *Communications Physics*, 4(1), 2021.

[69] Daniel Bothner, Ines C. Rodrigues, and Gary A. Steele. Four-wave-cooling to the single phonon level in Kerr optomechanics. *Communications Physics*, 5(1):1–10, 2022.

[70] Thomas Luschmann, Philip Schmidt, Frank Deppe, Achim Marx, Alvaro Sanchez, Rudolf Gross, and Hans Huebl. Mechanical frequency control in inductively coupled electromechanical systems. *Scientific Reports*, 12(1):1608, 2022.

[71] Jay Gambetta, Alexandre Blais, D. I. Schuster, A. Wallraff, L. Frunzio, J. Majer, M. H. Devoret, S. M. Girvin, and R. J. Schoelkopf. Qubit-photon interactions in a cavity: Measurement-induced dephasing and number splitting. *Physical Review A*, 74(4):042318, 2006.

[72] Alexandre Blais, Arne L. Grimsmo, S. M. Girvin, and Andreas Wallraff. Circuit quantum electrodynamics. *Reviews of Modern Physics*, 93(2):025005, 2021.

[73] P. Zhang, Y. D. Wang, and C. P. Sun. Cooling Mechanism for a Nanomechanical Resonator by Periodic Coupling to a Cooper Pair Box. *Physical Review Letters*, 95(9):097204, 2005.

[74] Marios Kounalakis, Yaroslav M. Blanter, and Gary A. Steele. Flux-mediated optomechanics with a transmon qubit in the single-photon ultrastrong-coupling regime. *Physical Review Research*, 2(2):023335, 2020.

[75] C. W. Gardiner and P. Zoller. *Quantum Noise*. 2004.

[76] G. Lindblad. On the generators of quantum dynamical semigroups. *Communications in Mathematical Physics*, 48(2):119–130, 1976.

[77] J. Krause, C. Dickel, E. Vaal, M. Vielmetter, J. Feng, R. Bounds, G. Catelani, J. M. Fink, and Yoichi Ando. Magnetic Field Resilience of Three-Dimensional Transmons with Thin-Film $\mathrm{AlAlO_x/Al}$ Josephson Junctions Approaching 1 T. *Physical Review Applied*, 17(3):034032, 2022.

[78] P. Forn-Díaz, L. Lamata, E. Rico, J. Kono, and E. Solano. Ultrastrong coupling regimes of light-matter interaction. *Reviews of Modern Physics*, 91(2):025005, 2019.

[79] Marius Bild, Matteo Fadel, Yu Yang, Uwe von Lüpke, Phillip Martin, Alessandro Bruno, and Yiwen Chu. Schrödinger cat states of a 16-microgram mechanical oscillator. *arXiv:2211.00449*, 2022.

[80] T. A. Palomaki, J. W. Harlow, J. D. Teufel, R. W. Simmonds, and K. W. Lehnert. Coherent state transfer between itinerant microwave fields and a mechanical oscillator. *Nature*, 495(7440):210–214, 2013.

[81] Ralf Riedinger, Andreas Wallucks, Igor Marinković, Clemens Löschnauer, Markus Aspelmeyer, Sungkun Hong, and Simon Gröblacher. Remote quantum entanglement between two micromechanical oscillators. *Nature*, 556(7702):473–477, 2018.

[82] R. W. Andrews, R. W. Peterson, T. P. Purdy, K. Cicak, R. W. Simmonds, C. A. Regal, and K. W. Lehnert. Bidirectional and efficient conversion between microwave and optical light. *Nature Physics*, 10(4):321–326, 2014.

[83] Moritz Forsch, Robert Stockill, Andreas Wallucks, Igor Marinković, Claus Gärtner, Richard A. Norte, Frank van Otten, Andrea Fiore, Kartik Srinivasan, and Simon Gröblacher. Microwave-to-optics conversion using a mechanical oscillator in its quantum ground state. *Nature Physics*, 16(1):69–74, 2020.

[84] Mohammad Mirhosseini, Alp Sipahigil, Mahmoud Kalaee, and Oskar Painter. Superconducting qubit to optical photon transduction. *Nature*, 588(7839):599–603, 2020.

[85] Jinwoong Cha, Kun Woo Kim, and Chiara Daraio. Experimental realization of on-chip topological nanoelectromechanical metamaterials. *Nature*, 564(7735):229–233, 2018.

[86] Amir Youssefi, Shingo Kono, Andrea Bancora, Mahdi Chegnizadeh, Jiahe Pan, Tatiana Vovk, and Tobias J. Kippenberg. Topological lattices realized in superconducting circuit optomechanics. *Nature*, 612(7941):666–672, 2022.

[87] J. D. Teufel, Dale Li, M. S. Allman, K. Cicak, A. J. Sirois, J. D. Whittaker, and R. W. Simmonds. Circuit cavity electromechanics in the strong-coupling regime. *Nature*, 471(7337):204–208, 2011.

[88] E. Verhagen, S. Deléglise, S. Weis, A. Schliesser, and T. J. Kippenberg. Quantum-coherent coupling of a mechanical oscillator to an optical cavity mode. *Nature*, 482(7383):63–67, 2012.

[89] Cristiano Ciuti and Iacopo Carusotto. Input-output theory of cavities in the ultrastrong coupling regime: The case of time-independent cavity parameters. *Physical Review A*, 74(3):033811, 2006.

[90] Cristiano Ciuti, Gérald Bastard, and Iacopo Carusotto. Quantum vacuum properties of the intersubband cavity polariton field. *Physical Review B*, 72:115303, 2005.

[91] Sebastian G. Hofer, Witlef Wieczorek, Markus Aspelmeyer, and Klemens Hammerer. Quantum entanglement and teleportation in pulsed cavity optomechanics. *Physical Review A*, 84(5):052327, 2011.

[92] Anton Frisk Kockum, Adam Miranowicz, Simone De Liberato, Salvatore Savasta, and Franco Nori. Ultrastrong coupling between light and matter. *Nature Reviews Physics*, 1(1):19, 2019.

[93] Sebastian G. Hofer and Klemens Hammerer. Entanglement-enhanced time-continuous quantum control in optomechanics. *Physical Review A*, 91(3):033822, 2015.

[94] Florian Marquardt, J. G. E. Harris, and S. M. Girvin. Dynamical Multistability Induced by Radiation Pressure in High-Finesse Micromechanical Optical Cavities. *Physical Review Letters*, 96(10):103901, 2006.

[95] Niels Lörch, Jiang Qian, Aashish Clerk, Florian Marquardt, and Klemens Hammerer. Laser Theory for Optomechanics: Limit Cycles in the Quantum Regime. *Physical Review X*, 4(1):011015, 2014.

[96] L. Bakemeier, A. Alvermann, and H. Fehske. Route to Chaos in Optomechanics. *Physical Review Letters*, 114(1):013601, 2015.

[97] C. Schulz, A. Alvermann, L. Bakemeier, and H. Fehske. Optomechanical multistability in the quantum regime. *Europhysics Letters*, 113(6):64002, 2016.

[98] P. Djorwe, Y. Pennec, and B. Djafari-Rouhani. Frequency locking and controllable chaos through exceptional points in optomechanics. *Physical Review E*, 98(3):032201, 2018.

[99] T. J. Kippenberg, H. Rokhsari, T. Carmon, A. Scherer, and K. J. Vahala. Analysis of Radiation-Pressure Induced Mechanical Oscillation of an Optical Microcavity. *Physical Review Letters*, 95(3):033901, 2005.

[100] Tal Carmon, M. C. Cross, and Kerry J. Vahala. Chaotic Quivering of Micron-Scaled On-Chip Resonators Excited by Centrifugal Optical Pressure. *Physical Review Letters*, 98(16):167203, 2007.

[101] F. M. Buters, H. J. Eerkens, K. Heeck, M. J. Weaver, B. Pepper, S. de Man, and D. Bouwmeester. Experimental exploration of the optomechanical attractor diagram and its dynamics. *Physical Review A*, 92(1):013811, 2015.

[102] Faraz Monifi, Jing Zhang, Şahin Kaya Özdemir, Bo Peng, Yu-xi Liu, Fang Bo, Franco Nori, and Lan Yang. Optomechanically induced stochastic resonance and chaos transfer between optical fields. *Nature Photonics*, 10(6):399–405, 2016.

[103] Daniel Navarro-Urrios, Néstor E. Capuj, Martín F. Colombano, P. David García, Marianna Sledzinska, Francesc Alzina, Amadeu Griol, Alejandro Martínez, and Clivia M. Sotomayor-Torres. Nonlinear dynamics and chaos in an optomechanical beam. *Nature Communications*, 8(1):14965, 2017.

[104] Rick Leijssen, Giada R. La Gala, Lars Freisem, Juha T. Muhonen, and Ewold Verhagen. Nonlinear cavity optomechanics with nanomechanical thermal fluctuations. *Nature Communications*, 8(1):ncomms16024, 2017.

[105] Junghyun Shin, Younghun Ryu, Mohammad-Ali Miri, Seung-Bo Shim, Hyoungsoon Choi, Andrea Alù, Junho Suh, and Jinwoong Cha. On-Chip Microwave Frequency Combs in a Superconducting Nanoelectromechanical Device. *Nano Letters*, 22(13):5459–5465, 2022.

[106] Mohammad-Ali Miri, Giuseppe D'Aguanno, and Andrea Alù. Optomechanical frequency combs. *New Journal of Physics*, 20(4):043013, 2018.

[107] Thales Figueiredo Roque, Florian Marquardt, and Oleg M. Yevtushenko. Nonlinear dynamics of weakly dissipative optomechanical systems. *New Journal of Physics*, 22(1):013049, 2020.

[108] A. P. Reed, K. H. Mayer, J. D. Teufel, L. D. Burkhart, W. Pfaff, M. Reagor, L. Sletten, X. Ma, R. J. Schoelkopf, E. Knill, and K. W. Lehnert. Faithful conversion of propagating quantum information to mechanical motion. *Nature Physics*, 13(12):1163–1167, 2017.

[109] Stefan Weis, Rémi Rivière, Samuel Deléglise, Emanuel Gavartin, Olivier Arcizet, Albert Schliesser, and Tobias J. Kippenberg. Optomechanically Induced Transparency. *Science*, 330(6010):1520–1523, 2010.

[110] I. S. Gradshteyn and I. M. Ryzhik. *Table of Integrals, Series, and Products.* Academic Press, Amsterdam, 7th edition, 2007.

[111] Marc Antoine Lemonde, Nicolas Didier, and Aashish A. Clerk. Nonlinear Interaction Effects in a Strongly Driven Optomechanical Cavity. *Physical Review Letters*, 111(5):053602, 2013.

[112] Bradley D. Hauer, Joshua Combes, and John D. Teufel. Nonlinear Sideband Cooling to a Schrödinger Cat State of Motion. *arXiv*, 2022.

[113] M. I. Dykman, Gianluca Rastelli, M. L. Roukes, and Eva M. Weig. Resonantly Induced Friction and Frequency Combs in Driven Nanomechanical Systems. *Physical Review Letters*, 122(25):254301, 2019.

[114] M. R. Vanner, I. Pikovski, G. D. Cole, M. S. Kim, Č Brukner, K. Hammerer, G. J. Milburn, and M. Aspelmeyer. Pulsed quantum optomechanics. *Proceedings of the National Academy of Sciences*, 108(39):16182–16187, 2011.

[115] H. Qiao, É. Dumur, G. Andersson, H. Yan, M.-H. Chou, J. Grebel, C. R. Conner, Y. J. Joshi, J. M. Miller, R. G. Povey, X. Wu, and A. N. Cleland. Splitting phonons: Building a platform for linear mechanical quantum computing. *Science*, 380(6649):1030–1033, 2023.

[116] Marius Bild, Matteo Fadel, Yu Yang, Uwe von Lüpke, Phillip Martin, Alessandro Bruno, and Yiwen Chu. Schrödinger cat states of a 16-microgram mechanical oscillator. *Science*, 380(6642):274–278, 2023.

[117] David Mason, Junxin Chen, Massimiliano Rossi, Yeghishe Tsaturyan, and Albert Schliesser. Continuous force and displacement measurement below the standard quantum limit. *Nature Physics*, 15(8):745–749, 2019.

[118] J.-M. Pirkkalainen, E. Damskägg, M. Brandt, F. Massel, and M. Sillanpää. Squeezing of Quantum Noise of Motion in a Micromechanical Resonator. *Physical Review Letters*, 115(24):243601, 2015.

[119] F. Lecocq, J. B. Clark, R. W. Simmonds, J. Aumentado, and J. D. Teufel. Quantum Nondemolition Measurement of a Nonclassical State of a Massive Object. *Physical Review X*, 5(4):041037, 2015.

[120] Soumya Ranjan Das, Sourav Majumder, Sudhir Kumar Sahu, Ujjawal Singhal, Tanmoy Bera, and Vibhor Singh. Instabilities near Ultrastrong Coupling in a Microwave Optomechanical Cavity. *Physical Review Letters*, 131(6):067001, 2023.

[121] S. Etaki, M. Poot, I. Mahboob, K. Onomitsu, H. Yamaguchi, and H. S. J. van der Zant. Motion detection of a micromechanical resonator embedded in a d.c. SQUID. *Nature Physics*, 4(10):785–788, 2008.

[122] D. Zoepfl, M. L. Juan, N. Diaz-Naufal, C. M. F. Schneider, L. F. Deeg, A. Sharafiev, A. Metelmann, and G. Kirchmair. Kerr Enhanced Backaction Cooling in Magnetomechanics. *Physical Review Letters*, 130(3):033601, 2023.

[123] Guillem Via, Gerhard Kirchmair, and Oriol Romero-Isart. Strong Single-Photon Coupling in Superconducting Quantum Magnetomechanics. *Physical Review Letters*, 114(14):143602, 2015.

[124] Lev S. Bishop, J. M. Chow, Jens Koch, A. A. Houck, M. H. Devoret, E. Thuneberg, S. M. Girvin, and R. J. Schoelkopf. Nonlinear response of the vacuum Rabi resonance. *Nature Physics*, 5(2):105–109, 2009.

[125] Lev S. Bishop, Eran Ginossar, and S. M. Girvin. Response of the Strongly Driven Jaynes-Cummings Oscillator. *Physical Review Letters*, 105(10):100505, 2010.

[126] S. S. Shamailov, A. S. Parkins, M. J. Collett, and H. J. Carmichael. Multi-photon blockade and dressing of the dressed states. *Optics Communications*, 283(5):766–772, 2010.

[127] J. M. Fink, L. Steffen, P. Studer, Lev S. Bishop, M. Baur, R. Bianchetti, D. Bozyigit, C. Lang, S. Filipp, P. J. Leek, and A. Wallraff. Quantum-To-Classical Transition in Cavity Quantum Electrodynamics. *Physical Review Letters*, 105(16):163601, 2010.

[128] Michael Fleischhauer, Atac Imamoglu, and Jonathan P. Marangos. Electromagnetically induced transparency: Optics in coherent media. *Reviews of Modern Physics*, 77(2):633–673, 2005.

[129] G. S. Agarwal and Sumei Huang. Electromagnetically induced transparency in mechanical effects of light. *Physical Review A*, 81(4):041803, 2010.

[130] Ross Shillito, Alexandru Petrescu, Joachim Cohen, Jackson Beall, Markus Hauru, Martin Ganahl, Adam G.M. Lewis, Guifre Vidal, and Alexandre Blais. Dynamics of Transmon Ionization. *Physical Review Applied*, 18(3):034031, 2022.

[131] Mehdi Abdi, Matthias Pernpeintner, Rudolf Gross, Hans Huebl, and Michael J. Hartmann. Quantum State Engineering with Circuit Electromechanical Three-Body Interactions. *Physical Review Letters*, 114(17):173602, 2015.

[132] Helin Zhang, Srivatsan Chakram, Tanay Roy, Nathan Earnest, Yao Lu, Ziwen Huang, D. K. Weiss, Jens Koch, and David I. Schuster. Universal Fast-Flux Control of a Coherent, Low-Frequency Qubit. *Physical Review X*, 11(1):011010, 2021.